Selective Tumor Hypoxia Targeting Using M75 Antibody Conjugated Photothermally Active MoO$_x$ Nanoparticles

Adriana Annušová,* Martina Labudová, Daniel Truchan, Veronika Hegedűšová, Helena Švajdlenková, Matej Mičušík, Mário Kotlár, Lenka Pribusová Slušná, Martin Hulman, Farnoush Salehtash, Anna Kálosi, Lucia Csáderová, Eliška Švastová, Peter Šiffalovič, Matej Jergel, Silvia Pastoreková, and Eva Majková

ABSTRACT: Photothermal therapy (PTT) mediated at the nanoscale has a unique advantage over currently used cancer treatments, by being spatially highly specific and minimally invasive. Although PTT combats traditional tumor treatment approaches, its clinical implementation has not yet been successful. The reasons for its disadvantage include an insufficient treatment efficiency or low tumor accumulation. Here, we present a promising new PTT platform combining a recently emerged two-dimensional (2D) inorganic nanomaterial, MoO$_x$, and a tumor hypoxia targeting element, the monoclonal antibody M75. M75 specifically binds to carbonic anhydrase IX (CAIX), a hypoxia marker associated with many solid tumors with a poor prognosis. The as-prepared nanoconjugates showed highly specific binding to cancer cells expressing CAIX while being able to produce significant photothermal yield after irradiation with near-IR wavelengths. Small aminophosphonic acid linkers were recognized to be more effective over the combination of poly(ethylene glycol) chain and biotin−avidin−biotin bridge in constructing a PTT platform with high tumor-binding efficacy. The in vitro cellular uptake of nanoconjugates was visualized by high-resolution fluorescence microscopy and label-free live cell confocal Raman microscopy. The key to effective cancer treatment may be the synergistic employment of active targeting and noninvasive, tumor-selective therapeutic approaches, such as nanoscale-mediated PTT. The use of active targeting can streamline nanoparticle delivery increasing photothermal yield and therapeutic success.
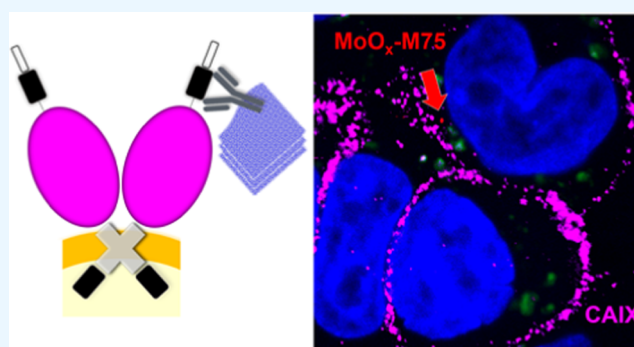
INTRODUCTION

Selective tumor-targeted therapies are becoming increasingly important for current cancer research.[1,2] Conventional treatment options do not account for preserving the healthy tissue surrounding the tumor or for off-target and adverse effects after treatment. In this sense, the involvement of nanosized biocompatible objects becomes intuitive. Given their dimensions, they are able to locally manipulate and control biochemical processes.[3−7] They can accumulate in target tissue based purely on their physicochemical properties.[1,8] On the other hand, conjugation of nanomaterials with functional biomolecules (enzymes, peptides, antibodies) is a way to confer advanced functions and unique properties to nano-complexes. This is called active targeting, which relies on the biological interaction between a targeting agent located on the surface of nanomaterials and a specific receptor existing on the cancer cell membrane.[1]

In our previous work, we have developed a new approach for active targeting involving antigen−antibody binding by linking nanomaterials with antibodies against the hypoxia biomarker Carbonic Anhydrase IX (CAIX).[9,10] CAIX is a glycoprotein

expressed on cancer cell membranes under hypoxic conditions.[11] It is involved in cell adaptation mechanisms to acidosis. CAIX expression can even promote progression toward malignancy and predict radio- and chemo-resistance.[12] Its expression on the cell membranes was revealed in many solid tumor types, such as colorectal, breast, lung carcinoma, carcinoma of reproductive organs, and head and neck carcinoma.[13] Its induction is stable, with a half-life of 38 h.[14] CAIX was identified 20 years ago by Pastoreková et al. using a monoclonal antibody (M75) in HeLa cell line.[15] Since then, M75 has been widely used for various immunodetection analyses in vitro, in vivo, and in tissues, and was proven as a functional targeting entity toward CAIX in hypoxic cells and tumor tissues.[16−20] M75 is highly specific against the repetitive

epitope within the extracellular proteoglycan domain of CAIX.[21] Thus, M75 as an active targeting agent on a nanosized platform can provide highly localized and selective delivery of therapeutic nanoagents to the desired tissue site. Using photoactive nanoparticles, we can mediate drug-free nanoscale photothermal cancer therapy with spatiotemporal controllability, *i.e.*, selective photothermal cancer therapy.

Currently, there is a wide range of nanomaterials suitable for PTT that are able to efficiently convert light to heat, ablate cancer cells, and induce local hyperthermia and tumor death. Besides noble metals, newly discovered alternatives like carbon-, semiconductor-, polymer-based, or two-dimensional (2D) layered nanomaterials have become a hot topic.[22,23] Emerging from the latter group, nonstoichiometric molybdenum oxides (MoO_x) are still waiting to reach their full potency. They are commonly prepared by the hydrothermal/solvothermal techniques[24−28] and liquid-phase exfoliation (LPE).[29,30] LPE, which was also used in this work, offers a certain advantage due to its ease of application and controllability. The starting material in this case is usually a microcrystalline molybdenum oxide powder. However, we have shown previously that MoO_x nanoparticles can also be prepared by spontaneous oxidation of MoS_2 nanoflakes in aqueous solution during LPE.[31,32]

MoO_x nanomaterials were first introduced as PTT agents in 2014 by Song et al.,[24] although many studies have previously reported the existence of localized surface plasmon (LSP) resonance in MoO_x-based nanomaterials, see, *e.g.*, ref 33. Several studies followed shortly thereafter, drawing attention to its powerful photothermal effect, demonstrated both on *in vitro* and *in vivo* biological models.[25,26,34−39] Indeed, MoO_x present an exciting option as in addition to low cost, high stability, low clustering, and easy fabrication, a change in their LSP resonance can be induced independently of their size and shape.[40,41] MoO_x with suitable morphology and degree of oxidation show strong LSP in the near-IR region.[24,42−44] Scattering and absorption by tissue are low at these wavelengths, meaning increased penetration depth of radiation that allows deep tissue therapeutic options.

To the best of our knowledge, the conjugation of MoO_x with highly selective active targeting moieties has not yet been reported in the literature, and its potential for therapy remains to be explored. The work of Qiu et al. describes the functionalization of MoO_x with folic acid (FA) used for combined chemo-photothermal therapy.[45] The MoO_x nanoparticles were synthesized by a hydrothermal procedure and dual conjugated with NH_2 bearing pegylated lipoic acids and FA-modified bovine serum albumin (BSA), resulting in a lateral size of 90 nm, thickness of 3 nm, and ζ potential of −17.5 mV. The FA-BSA-PEG/MoO_x complexes loaded up to 76.49% with chemotherapy agent docetaxel (DTX) showed to be more effective than the commercial drug Taxotere. Although folic acid is a targeting ligand to folate receptors that are overexpressed in various tumor cells, they also occur naturally in various types of healthy cells.[46] Targeting via CAIX is more selective because it is almost exclusively expressed in tumors, and we attack it with an antibody, which is the most specific targeting method. Other *in vivo* studies involving MoO_x-based nanomaterials have relied on the enhanced permeation and retention effects to induce accumulation at tumor sites after intravenous injection and/or injection directly into the cancerous lesions.

In the present paper, MoO_x-M75 nanoconjugates were assembled using two conjugation schemes involving (i) small organic aminophosphonic acid linkers, 3-aminopropylphosphonic acid (APPA), and 4-aminobutylphosphonic acid (ABPA); and (ii) the biotin−avidin−biotin bridge, known as the strongest noncovalent interaction in biochemistry, with 2 kDa poly(ethylene glycol) (PEG). PEG was used in our previous studies to link M75 antibody to pegylated MoS_2[9] and graphene oxide (GO)[10] nanoflakes, already demonstrating the potential behind M75-guided NP delivery to tumor sites. However, the nanomaterials coating influences protein corona formation, toxicity, biocompatibility, and the circulation time of the platform in the bloodstream. This necessitates the evaluation of the effect of different linkers on the nanoconjugates in biological models. The most commonly used coating for MoO_x nanoparticles so far is PEG.[34,35,37,38] Alternatively, we were inspired by numerous studies investigating the binding of phosphonate-based low-molecular-weight molecules to metal oxide surfaces.[47−51] They form stable bonds with inorganic molecules and can be used to prepare self-assembled monolayers (SAM) on planar substrates.[47,52−58] In contrast to the well-known silane-based molecular couplers, *e.g.*, 3-aminopropyltriethoxysilane (APTES), they exhibit higher stability in physiological conditions and are not prone to uncontrollable polymerization.[47,51] In our study, we also benefited from the water-soluble properties of APPA and ABPA, which, compared to the use of APTES, facilitated the NP functionalization with −NH_2 groups. Despite many studies, the use of these linkers compared to PEG in the context of nanoparticles or biomolecules anchored to nanoparticles has not yet been fully explored in the literature. He et al. prepared graphene oxide (GO)-modified aluminum powder using APPA to improve the anticorrosive properties of the powder.[59] APPA was used in the work of Tudisco et al. to modify magnetic Fe_3O_4 nanoparticles (MNPs) with β-cyclodextrin (β-CD),[60] while the efficiency of the anchoring group on MNPs, phosphonic acid over ester, was also investigated.

In this work, we demonstrate the selective targeting of tumor hypoxia using an M75 antibody recognizing hypoxia biomarker CAIX, and photothermal MoO_x-M75 nanoparticle conjugates. To the best of our knowledge, MoO_x NP conjugates are considered here for the first time as active targeting platforms demonstrating specific antigen−antibody recognition. The paper initially details the MoO_x nanoparticles and bioconjugate preparation and characterization, particularly emphasizing their morphological, optical, and photothermal properties. Small MoO_x nanoparticles with an average diameter of 4 nm were prepared by the LPE method, starting from MoO_2 powder, and consequently bioconjugated using a novel approach involving small aminophosphonic molecules or the biotin−avidin−biotin binding scheme with the well-known PEG chain. In parallel, their stability, optical properties, and cellular interactions were studied. Statistically relevant flow cytometry measurements served to quantify the conjugate's tumor-binding selectivity first in model cell lines, C33 CAIX and C33 neo, the former derived to express high levels of CAIX antigens while the latter being CAIX negative, as well as in hypoxically preincubated cancer cell lines showing natural expression of the CAIX antigen. In addition, the conjugate internalization in cancer cells is visualized via live cell label-free confocal Raman microscopy (CRM) and fluorescently labeled microscopy
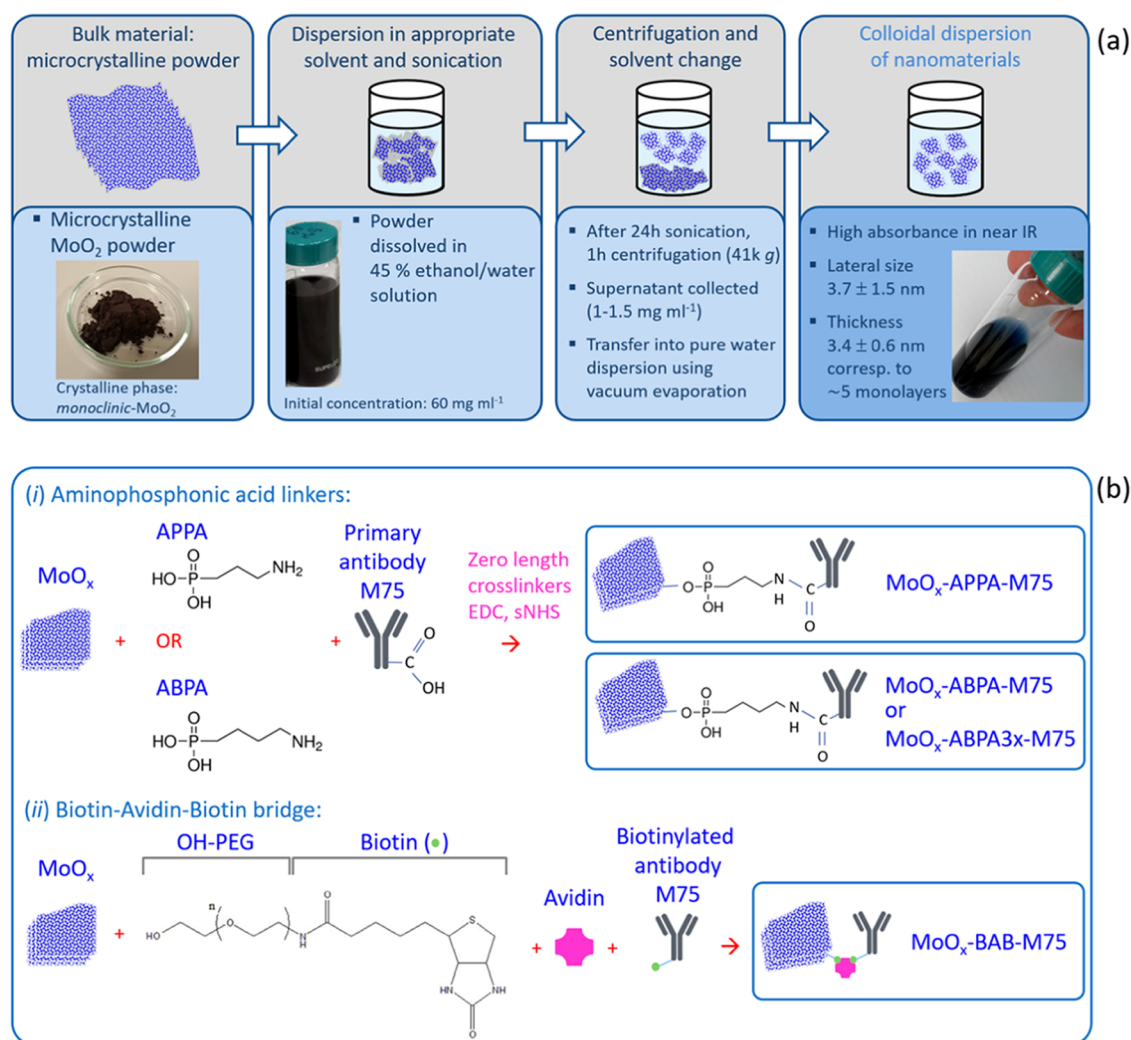
Figure 1. Scheme of the MoO$_x$ nanoparticles exfoliation process in liquid phase (a) and the preparation of the MoO$_x$-M75 conjugates (b), using small organic molecules (i) and the biotin−avidin system (ii).

techniques including high-resolution stimulated emission depletion microscopy (STED) measurements.

RESULTS AND DISCUSSION

Nanoparticle Synthesis and the Bioconjugation Process. MoO$_x$ nanoparticles were synthesized by a liquid-phase exfoliation technique. The synthesis scheme is illustrated in Figure 1a. Briefly, the process consisted of the sonication and subsequent centrifugation of a certain amount of microcrystalline MoO$_2$ powder dissolved in a 45% ethanol/water solution. For more details, see the Supporting Information. The pH of the resulting aqueous nanoparticle solution is acidic, with a value of around 3.12. At this pH, the solution retains its original absorption properties and colloidal stability over time. The concentration yield after exfoliation is on average 1−1.5 mg mL^{-1}, while a concentration of 3 mg mL^{-1} was used for conjugation with antibodies.

M75 antibody was linked to MoO$_x$ nanoparticles using either aminophosphonic acid linkers or the biotin−avidin−biotin bridge. To compare the efficacy of different linkers, the same amount of antibody was used per batch. The functionalization protocols are shown in Figure 1b and are detailed in the Supporting Information. The various linkers and biomolecules were added progressively, and at certain

molar ratios. To remove the unbound molecules, intermittent dialysis steps followed. For both conjugation schemes, we consider the presence of reactive −OH groups on the nanoparticles surface. For the first type of conjugates, two organophosphonic molecule linkers bearing NH$_2$ groups were used: 3-aminopropylphosphonic acid (APPA) and 4-amino-butylphosphonic acid (ABPA), having slightly different molecular weights of 139.09 and 153.12 Da, respectively. Through the NH$_2$ group, the antibody M75 was linked to a covalent bond. The conjugates with and without M75 are labeled "MoO$_x$-APPA", "MoO$_x$-ABPA", "MoO$_x$-APPA-M75", "MoO$_x$-ABPA-M75", and "MoO$_x$-ABPA3x-M75", respectively. Note that "MoO$_x$-ABPA3x-M75" has a 3 times higher molar ratio of ABPA over MoO$_x$ (see also the Supporting Information). In the second type of nanoconjugate, first, we linked poly(ethylene glycol) (PEG) to MoO$_x$, with a molecular weight of 2 kDa and terminated at one end with a biotin molecule (244 Da). The PEGylated particles are labeled "MoO$_x$-PEG". Biotinylated M75 antibodies were function-alized on the surface of MoO$_x$ by the addition of avidin (68 kDa), labeled "MoO$_x$-BAB-M75".

The bioconjugates' pH after the last dialysis step is 4.5 ± 0.1 (averaged values for MoO$_x$-APPA-M75, MoO$_x$-ABPA-M75, MoO$_x$-ABPA3x-M75, and MoO$_x$-BAB-M75). The dialysis step
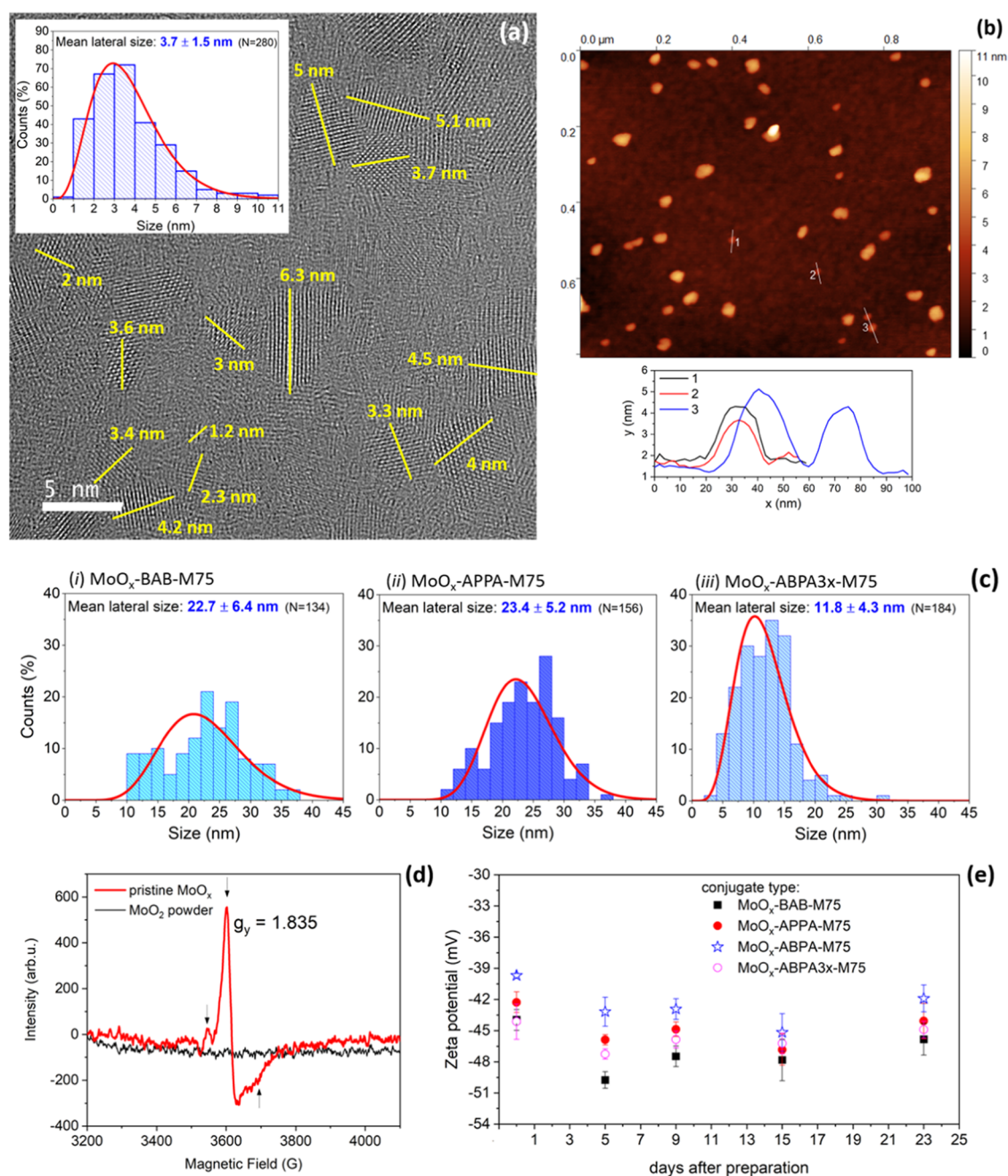
Figure 2. TEM image of pristine MoO_x nanoparticles, with size distribution histogram in inset (a). AFM image of pristine MoO_x nanoparticles with line profiles (b). Lateral size distribution histograms of the nanoconjugates (c) with MoO_x-BAB-M75 (i), MoO_x-APPA-M75 (ii), and MoO_x-ABPA3x-M75 (iii). Comparison of the electron paramagnetic resonance (EPR) spectrum of pristine MoO_x nanoparticles and MoO_2 microcrystalline powder (d). The EPR spectrum is the first derivative of the absorption spectrum. The point at which the spectrum passes through zero corresponds to the maximum absorption of electromagnetic radiation. Colloidal stability of the different MoO_x-M75 nanoconjugates (e).

itself causes an increase in pH. It is not an effect observed due to the conjugation process. Dialyzed pure MoO_x solution has a pH of 4.55. For some experiments detailed further, we also prepared OH−PEG−biotin and ABPA dissolved in pure deionized water as well as conjugates BAB-M75 and ABPA-M75 without the MoO_x nanoparticles.

Morphology and Colloidal Stability. Figure 2 shows examples of transmission electron microscopy (TEM) and atomic force microscopy (AFM) images of the MoO_x nanomaterials. The lateral size distribution was assessed by TEM measurements. Statistics on 280 nanoparticles revealed a

mean particle size of 3.7 ± 1.5 nm. A mean thickness was determined from AFM measurements (see image and corresponding line profiles in Figure 2b), which was found to be 3.4 ± 0.6 nm, which corresponds to around 5 monolayers of MoO_x.[61,62]

The size of the nanoconjugates was evaluated by AFM measurements. Examples of AFM images can be found in Figure S1, while Figure 2 shows the resulting size distributions. The conjugate diameter was increased after functionalization, confirming the addition of bioelements and linkers. A mean lateral size of 22.7 ± 0.6, 23.4 ± 0.6, and 11.8 ± 4.3 nm was

found for MoO$_x$-BAB-M75, MoO$_x$-APPA-M75, and MoO$_x$-ABPA3x-M75, respectively. The mean thickness was found to be 3.0 ± 0.3, 3.0 ± 1.4, and 1.7 ± 0.2 nm, respectively. Examples of AFM images with line profiles of the bioconjugates are shown in Figure S1a–c, see the Supporting Information.

Grazing-incidence X-ray diffraction (GIXRD) measurements revealed that the prepared nanoparticles crystalline phase can be assigned to hexagonal molybdenum trioxide (h-MoO$_3$) with a lattice parameter expanded by 0.41% compared to the PDF2-ICDD database, see Figure S2a. Note that the MoO$_2$ microcrystalline powder from which the nanoparticles are exfoliated, can be characterized by a monoclinic molybdenum dioxide (m-MoO$_2$) phase, see Figure S2b, which is considered thermodynamically more stable than a hexagonal one, which is known to be metastable. This means that the exfoliation process leads to rearranging of the unit cell, which is not common in crystallography.

In the literature, it is common to label a specific molybdenum oxide crystalline phase in nanomaterial with the LSP resonance effect as a nonstoichiometric molybdenum oxide (MoO$_x$). This notation refers mainly to the presence of the LSP resonance effect in the material. The LSP resonance effect arises due to free electrons in the crystals generated by charge transfer processes within different valence states of Mo (Mo^{5+}, Mo^{6+}).[42] The presence of free electrons or unpaired electrons and thus the existence of localized plasmons were elucidated by EPR experiments. Figure 2d compares the obtained EPR spectra for the MoO$_2$ microcrystalline powder and MoO$_x$ pristine nanoparticles. In the case of the MoO$_x$ nanoparticles, we can observe multiple distinguishable peaks attributable to paramagnetic centers. The appearance of the main (center) peak at g_y = 1.835 and two less intense peaks compared to the reference MoO$_2$ sample confirms a formation of paramagnetic Mo^{5+} species in the MoO$_x$ sample.[63,64] Free electrons can localize to form these centers and, hence, oxygen vacancies. Thus, we can conclude that the prepared MoO$_x$ nanomaterials indeed possess photothermal properties due to LSP. The strong absorption peak in the near-IR (see below) can be attributed to LSP, which increases the electromagnetic field and results in a rapid heating effect after near-IR laser irradiation. X-ray photoelectron spectroscopy (XPS) measurements support our findings, as shown in Figure S3 and Table S1. MoO$_2$ powder exhibits a strong Mo 3d$_{5/2}$ signal at 229.7 eV corresponding to Mo^{4+} species, while in the case of MoO$_x$ samples, mostly signal from Mo^{6+} (Mo 3d$_{5/2}$ at ca. 233.5 eV) accompanied by a small fraction of Mo^{5+} signal (Mo 3d$_{5/2}$ at ca. 232.2 eV) is detected.

We ascertained the stability of the prepared MoO$_x$ colloidal solutions by using ζ potential measurements. The ζ potential of the pristine MoO$_x$ nanoparticles is equal to −50 ± 7 mV; hence, high colloidal stability can be attributed to this material resulting from the LPE process. In fact, the solution does not aggregate or precipitate in aqueous solution. The only limiting factor is color fading. It is probably caused by oxidation in water.[39,45] However, this effect starts to show only after about a month. Until then, the solution retains its original absorption properties and dark blue color as well as its original ζ potential value within the displayed standard deviation. Regarding the colloidal stability of the different nanoconjugates, we measured the ζ potential for an individual batch over 3 weeks after the particles functionalization. Figure 2 shows the ζ potential values for the four conjugate types as a function of time. After

the last dialysis, the ζ potential is equal to −44 ± 1, −42 ± 1, −40 ± 1, and −44 ± 2 mV for MoO$_x$-BAB-M75, MoO$_x$-APPA-M75, MoO$_x$-ABPA-M75, and MoO$_x$-ABPA3x-M75, respectively. All conjugate types show long-term colloidal stability with a slight decrease in ζ potential compared to that of pristine MoO$_x$. Therefore, we can conclude that the APPA and ABPA organophosphonic molecules are equally effective in rendering the MoO$_x$ nanomaterials colloidally stable compared with the more common PEG-based coatings.

Confirmation of the Conjugation Process. In order to confirm that the particles are functionalized according to the proposed schemes, we conducted optical spectroscopy measurements in the near-IR region. The water forms a tetrahedral flexible hydrogen bond network and can be considered as a probe reflecting the changes within the solution. This is a relatively novel scientific discipline dealing with the interactions of water and light called aquaphotomics.[65,66] Chatani et al. used the transformations within the water spectral patterns to study the nucleation-dependent fibrillation of insulin in real time.[67] Tsenkova et al. monitored aqueous solutions of prion proteins binding Cu and Mn using near-IR spectroscopy.[68] Our work points out the potential of near-IR spectroscopy in monitoring the formation of MoO$_x$-M75 conjugates by using hydrogen bonds. We applied this technique to two conjugate types, ABPA-based, and the combination of PEG and the biotin−avidin−biotin bridge. The spectrum of water exhibited three absorption regions at 8403.4, 6896.5, and 5154.6 cm^{-1}, see Figures S4−S7 in the Supporting Information, attributed to the combination of the first overtone of the OH stretching and OH bending band, the first overtone of the OH stretching band and the combination of the OH stretching and OH bending band, respectively.[69] The cluster-like water structures including hydration shell and hydrogen species were revealed via decomposition of the OH stretching band (6000−7700 cm^{-1}) into six Gaussian fit curves consisting of water clusters with four down to one hydrogen bonds (I−IV), free OH (V) and the rotation mode of OH groups (VI), see Figures S4−S6. Changes observed in this region at different stages of the functionalization process are the first indications of preferential interactions among the nanoparticle, the linkers, and the biomolecules, after their addition. Next, the formation of MoO$_x$-PEG and MoO$_x$-ABPA conjugates as well as the MoO$_x$-BAB-M75 and MoO$_x$-ABPA-M75 conjugates was observed by the appearance of the absorption band around or below 7800 cm^{-1} and the significant increase of the absorption at 9000 cm^{-1}, see Figure S7. This study first confirmed the formation of conjugates during the functionalization process. Second, it showed the different nature of the aminophosphonic acid linker-based scheme and the combination of PEG and biotin−avidin−biotin-based schemes. Below, we show that this difference also affects the *in vitro* results concerning the conjugate's binding and internalization in cells.

FTIR measurements performed on the same conjugate types confirmed the conclusion of the near-IR study; see Figure S8. The MoO$_x$ peaks in the low-wavenumber range are present for all conjugate types or overlap with the peaks belonging to the individual linkers: MoO$_x$-PEG, MoO$_x$-BAB-M75, MoO$_x$-ABPA, MoO$_x$-ABPA-M75. M75 was identified based on the presence of Amide I and Amide II peaks in both the MoO$_x$-BAB-M75 and MoO$_x$-ABPA-M75 conjugates spectrum.

Further confirmation of the conjugation process is provided by XPS measurements of the PEG- and APPA-based samples; see Figures S9 and S10 and Table S2. XPS revealed the signal
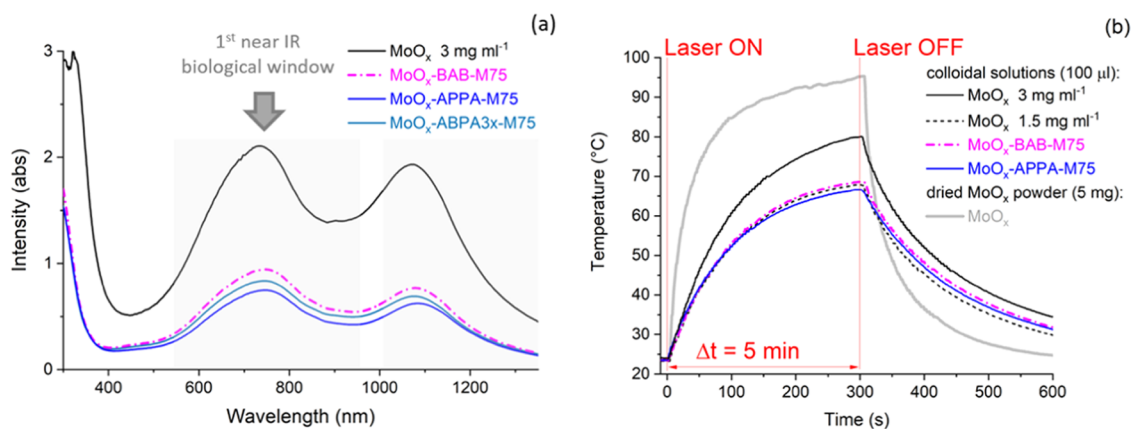
Figure 3. Absorbance curve of the liquid-phase exfoliated MoO_x nanoparticle solution and conjugates MoO_x-BAB-M75, MoO_x-APPA-M75, and MoO_x-ABPA3x-M75 (a). Heating effect and consequent cooling of MoO_x nanoparticle solutions of different concentrations, compared with the bioconjugated samples as well as with dried MoO_x nanoparticle powder (b).

for P 2p core-level state in MoO_x-APPA, and the C−O signal increase in MoO_x-PEG, typical of the PEG chain. Nitrogen was also detected on the surface, confirming the presence of M75 antibodies in MoO_x-BAB-M75 and MoO_x-ABPA-M75.

Optical and Photothermal Properties. The absorbance curves of the MoO_x nanoparticle solution as well as MoO_x-BAB-M75, MoO_x-APPA-M75, and MoO_x-ABPA3x-M75 conjugates are shown in Figure 3a (measured at the mentioned pH of 4.5 ± 0.1). Strong absorption properties in the near-IR region can be ascribed to the present solutions. Moreover, it can be seen that the conjugation process results in a minor decrease of the absorbance intensities compared to the starting solution. This can be attributed to the fact that the conjugation process requires further addition of small amounts of liquid (dilution) to the original MoO_x colloidal solution. The dialysis process can result in some particle loss, as well. While the increase of pH after dialysis from 3.12 to 4.5 can have an effect too. We investigated how the absorption properties are altered after a change of the solutions' pH, for more details, see the Supporting Information and Figures S11a−c. The acidic pH favors high near-IR absorption. A rather abrupt fall in the absorbance between 5.18 and 5.4 is manifesting. After 5.4, the solution becomes light blue, showing a decreased ability to absorb near-IR light. Our results are in accord with previous studies. MoO_x-based nanoparticles as pH-responsive functional elements have been studied by several groups.[45,70−72]

In addition to the pH dependence, slight changes in the MoO_x nanoparticles absorption can also be observed by using microcrystalline powders with different elemental compositions (even trace elements can have an effect), see Figure S12. Indeed, the shape, width, and exact positions of the near-IR absorbance peak's maxima (±10−20 nm) differ in the available literature, which is understandable given the different preparation methods and materials. In our case, when examining the exfoliation yield of MoO_x from different MoO_2 powders, we noticed that the second near-IR peak at about 1075 nm appears to be most affected. The first near-IR peak always had the highest absorbance values in this range. The investigation of this phenomenon is not the subject of this paper. However, this influenced the choice of the laser wavelength at which the photothermal properties were studied.

The photothermal properties of the MoO_x nanoparticles are demonstrated by measurements of the heating effect upon laser irradiation by an 808 nm laser diode. Figure 3b shows this

curve for both the starting solutions and the MoO_x conjugates. In the case of the starting solutions with concentrations of 1.5 and 3 mg mL^{-1} (0.15 and 0.3 mg MoO_x nanoparticles in the irradiated samples, respectively), the temperature increase upon 5 min laser irradiation with 808 nm was 44 and 53 °C, respectively. The slope of the temperature increase is steeper for the 3 mg mL^{-1} sample, but the cooling rate is similar to that for 1.5 mg mL^{-1} and conjugated samples. This shows that a more concentrated MoO_x solution has a higher absorbance but the same heat capacitance as the less concentrated samples. We recall that the conjugated solutions were prepared using the 3 mg mL^{-1} concentration starting solution. After irradiation of the MoO_x-BAB-M75 and MoO_x-APPA-M75 samples, the temperature increase is 45 and 43 °C, respectively, i.e., at the level of the 1.5 mg mL^{-1} sample. The changes in the heating efficiency after the conjugation process are expected as the absorbance decreases (Figure 3a). However, the conjugation process does not result in significant changes in heat conservation after irradiation (slope of the temperature decrease after 300 s is not substantially altered, see black dashed curve vs magenta and blue). Figure 3b also contains the heating curve for dried MoO_x powder compared to the colloidal solutions. We can notice that the heating effect slows down after 1 min of irradiation. After 5 min of irradiation, the temperature increases from 71.5 to 95 °C. The cooling of the dried nanoparticle powder is more rapid, compared to the colloidal solutions, caused by the high heat capacity of water. We conclude that MoO_x nanoparticles prepared by LPE and MoO_x-M75 nanoparticle conjugates can be considered as photothermal therapeutic agents.

Nanoconjugates Effect on Cell Viability and Their Uptake by Cancer Cells. Figure 4a presents the cell viability response upon 24 h of incubation at 120 μg/well (i.e. 860 μg mL^{-1}) with pristine MoO_x and nanoconjugates in the case of the main model cell lines, C33 CAIX and C33 neo, as well as for different hypoxically preincubated cancer cell lines, A549, BxPC3, COLO357, FaDu, HCT116, JIMT-1. The C33 CAIX is the cervical cancer cell line C33A, stably transfected with pSG5C-MN/CA9 plasmid to express high levels of CAIX. While C33 neo is the control cell line, with negligible CAIX antigen expression. No significant decrease in the viability values was observed. Nevertheless, the conjugate MoO_x-BAB-M75 in A549, FaDu, and JIMT-1 shows a greater negative impact on cell viability. JIMT-1 is also affected by the
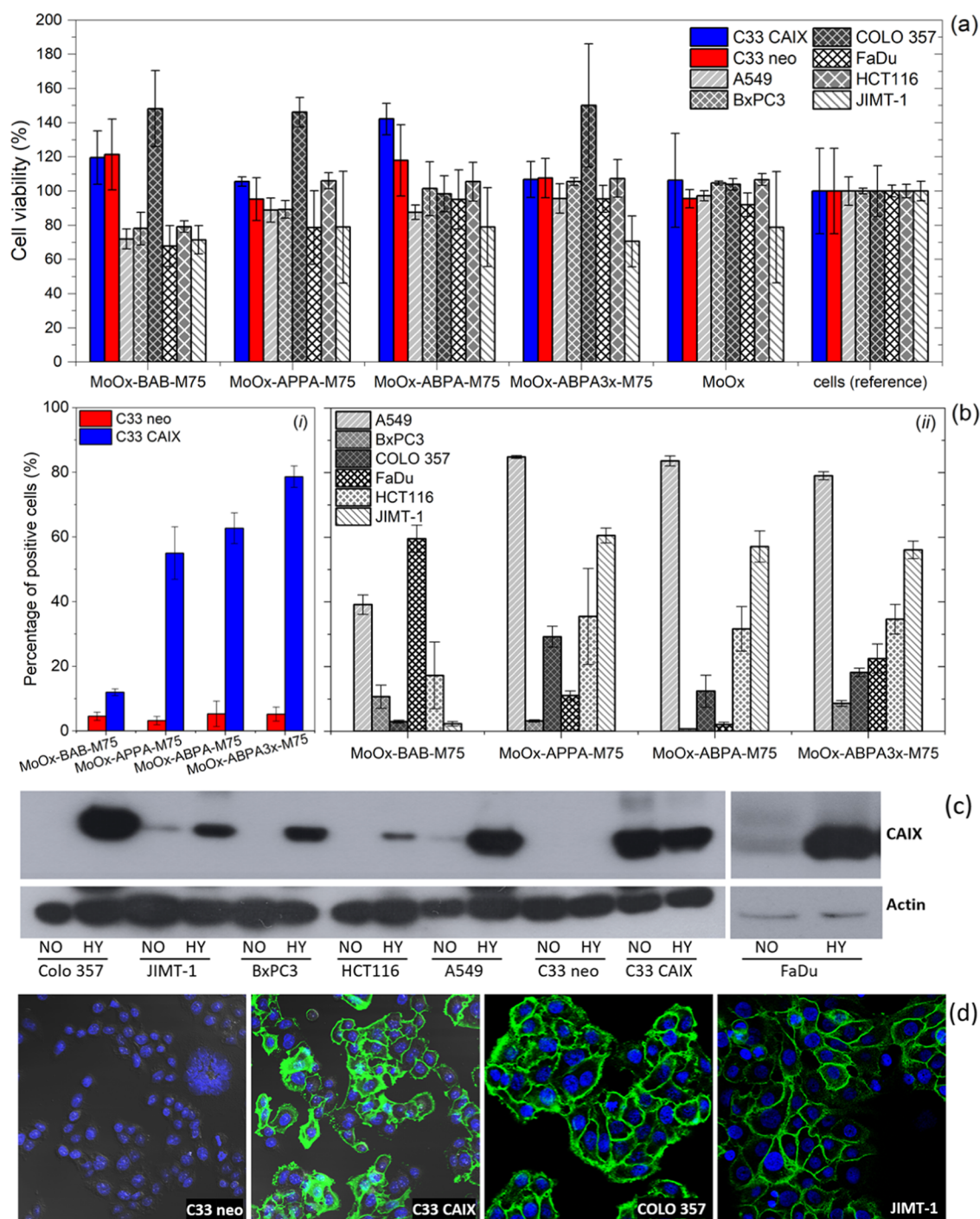
Figure 4. Cell viability results after 24 h of incubation with different MoO_x-M75 bioconjugates (120 μg/well) (a). The viability values are normalized to the reference cells per individual cell lines. Cellular uptake of MoO_x bioconjugates by model cell lines C33 CAIX and C33 neo, as well as multiple hypoxically preincubated cancer cell lines (b). For controls, see Figure S13. Western blot analysis of CAIX levels in different cell lines used (c). All of the cell lines were incubated under normoxic (NO) and hypoxic (HY) conditions. β-Actin was used as a loading control. (d) Representative images of CAIX expression and localization in selected cell lines. C33 neo cells are CAIX negative, C33 CAIX, and hypoxically preincubated COLO 357 and JIMT-1 exhibit a strong cell surface CAIX localization. CAIX was visualized using immunofluorescent staining by M75 antibody and anti-mouse Alexa Flour 488 conjugated secondary antibody (green), nuclei were stained by DAPI (blue).

conjugate MoO_x-ABPA3x-M75. In these cases, the viability falls below 75%. On the other hand, certain cell line viability increases above 100%. This cell overgrowth can be frequently observed in biocompatible nanomaterials.[9,73] The high biocompatibility of the MoO_x and MoO_x-M75 conjugates studied herein is consistent with the literature on MoO_x-based nanomaterials. MoO_x-PEG nanoparticles incubated for 24 h

with HeLa, HepG2, and PANC-1 cells showed cell viability as high as 82% up to a concentration of 200 μg mL^{-1}.[37] Song et al. incubated MoO_x-PEG with 4T1 cells from 0 to 100 μg mL^{-1}, resulting in a no lower than an 80% viability at 100 μg mL^{-1}.[35] Odda et al. demonstrated very low cytotoxicity of Prussian blue functionalized MoO_x in human triple-negative breast cancer cell lines, 4T1, corresponding to only a 5%
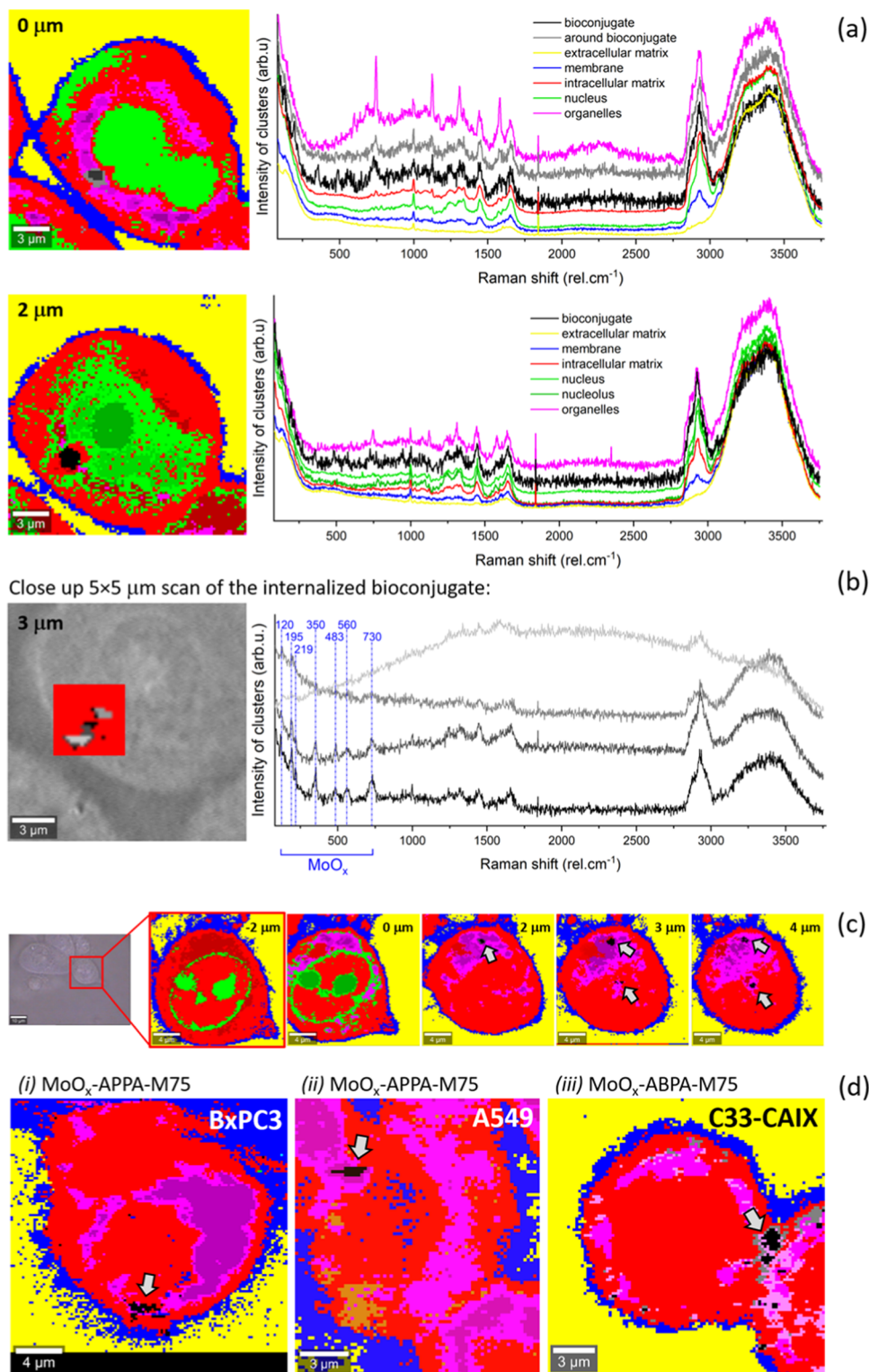
Figure 5. Results of CRM live cell imaging after 24 h of incubation with nanoconjugates. MoO_x-BAB-M75 nanoconjugate with JIMT-1 cells (a−c) and aminophosphonic acid linker-based conjugates with different cancer cell lines (d): MoO_x-APPA-M75 in BxPC3 (i) and A549 (ii), and MoO_x-ABPA-M75 in C33 CAIX (iii). The bright-field images depict the scanned areas of the cell monolayers. The color-coded 2D images with the corresponding spectra (added in some cases) show the identified clusters denoting different cell parts, while identifying the internalized bioconjugate. The spectra were scaled to provide more clarity. (a) Single cell at two different focal planes separated by 2 μm. (b) Close-up scan on the bioconjugate at the focal plane $Z = 3$ μm. The red color on the bright-field image of (b) denotes the intracellular space (spectrum not included). The MoO_x peaks are indicated by blue vertical lines in the diagram in (b). (c) Example of three-dimensional (3D) live cell imaging of a single cell. The Z-scan levels are indicated in the top right corner of the images. The arrows mark the position of the nanoconjugates at $Z = 0, -2$, and -4 μm, located within cell organelles. (d) Identified aminophosphonic acid linker-based nanoconjugates internalized in cells, marked by arrows.

decrease in viability for all concentrations up to 250 μg mL^{-1}.[39]

Flow cytometry measurements quantitatively assessed the conjugates' selective targeting abilities (Figure 4b). Note that all of the cell lines below were cultured under hypoxia and the addition of nanoparticle solution to the cell media at a concentration of 120 μg/well (*i.e.* 860 μg mL^{-1}) caused no changes in the overall pH of the cell cultures even after a 24 h incubation period. In the first place, we studied the model cell lines, C33 CAIX and C33 neo (see (i)), as they provide straightforward information about the selective nature of the prepared conjugates. There are significant differences in the binding levels between C33 CAIX and C33 neo, not exceeding 5% in the latter. Given that C33 neo are cells that show no expression of CAIX at all,[74] the exclusively CAIX-directed activity of the MoO$_x$-M75 bioconjugates is confirmed. Indeed, we can conclude that around 95% of the conjugate uptake is governed by the antigen−antibody binding. Moreover, we can also highlight the importance of organophosphonic acid linkers as the MoO$_x$-BAB-M75 conjugate positivity in C33 CAIX is 12 ± 1%, while in the case of MoO$_x$-APPA-M75, MoO$_x$-ABPA-M75, and MoO$_x$-ABPA3x-M75, the binding levels are equal to 55 ± 8, 63 ± 5, and 79 ± 5%, respectively. The slightly higher molecular weight of the ABPA molecule, as well as its increased molar ratio versus MoO$_x$ nanoparticles, appears to make the nanoconjugate more attractive for uptake by C33 CAIX compared to the APPA-based one.

Next, multiple hypoxically preincubated cancer cell lines: A549, BxPC3, COLO357, FaDu, HCT116, and JIMT-1, were tested (see (ii) on Figure 4b). We remind, that compared to these cells, the C33 CAIX is a model cell line designed to express exceptionally high levels of CAIX, independently of hypoxic preincubation. Cell lines A549 and JIMT-1 display significant uptake of the organophosphonic molecule-based conjugates, with positivity reaching around 82 and 57%, respectively. The differences in intake of the PEG-based vs aminophosphonic acid linker-based conjugates are similar for these two cell lines, being around 43 and 56%, respectively. However, COLO 357 and HCT116 show minor discrepancies in this sense, while the former is more sensitive than HCT116 to the aminophosphonic acid linker-based conjugate type. On the other hand, the highest binding levels of the conjugate MoO$_x$-BAB-M75 can be found in FaDu cell line, while BxPC3 demonstrates relatively low activity to all MoO$_x$-M75 conjugates. These results corroborate that different coatings lead to diverse interactions of nanoparticles with cells, influencing their uptake, transport, and exclusion. Our work points out the potential behind the aminophosphonic acid-based MoO$_x$-M75 conjugate types as active targeting entities. The expression of CAIX in the studied cell lines is verified by Western blot analysis; see Figure 4c. Most of the cell lines used do not express CAIX or only at very low levels under normoxic conditions. As CAIX expression is strongly regulated by hypoxia, all investigated cell lines show considerably higher levels of this protein after hypoxic preincubation. Representative immunofluorescent images document hypoxia-induced CAIX expression in COLO 357 and JIMT-1 localized on plasma membrane; see Figure 4 (d). The immunofluorescence analysis proves CAIX negativity of C33 neo and shows high levels of CAIX in transfected C33 CAIX cells.

Nanoconjugates *In Vitro* Cellular Localization. The cellular uptake of the MoO$_x$-M75 conjugates presented here was further proven by label-free CRM and fluorescently labeled CLSM and STED measurements. It should be noted that these methods do not serve as statistical references compared to flow cytometry. However, they help to visualize, track, and localize the conjugates inside the intracellular space.

The method of label-free live cell CRM allows the study of living cells in their natural environment without the use of fluorescent dyes. Label-free CRM has been successfully applied in biomaterials investigations in recent years.[75−83] Conventional fluorescent labels could be invasive and induce cell cytotoxicity, while photobleaching can cause the decomposition of fluorescent molecules, leading to a reduction in the fluorescent signal and the formation of free radicals and other highly reactive and toxic substances.[84] Label-free live cell CRM enables real-time detection of bioconjugated nanoparticles in the intracellular space with submicrometric resolution, as well as differentiation of individual cell compartments.[81,83] By application of cluster analysis to the recorded spectra, individual cellular parts and the functionalized MoO$_x$ nanoparticles can be identified. Prior to cluster analysis, Principal Component Analysis (PCA) can be performed to reduce the dimensionality and lower the hyperspectral data noise. In our previous studies, we successfully visualized MoS$_2$-[9,85] and GO-based[10,73] nanoflakes inside cellular matter using this method. The conjugates were localized in lysosome-rich cellular regions. Moreover, we used the method of label-free live cell CRM to assess the HaCaT human keratinocyte cell line morphological changes induced by essential oils encapsulated in poly(ε-caprolactone) nanocapsules.[86] We showed the existence of lipoprotein aggregates within cells, which is in agreement with concentration-dependent cytotoxicity studies.

Figure 5a shows false color-coded images with corresponding spectra of the same cell imaged at two different Z focal planes ($Z = 0$ and 2 μm, where 0 is a relative designation of the first focal plane). The measurements were realized on a live JIMT-1 cell line after 24 h of incubation with MoO$_x$-BAB-M75 nanoconjugates. The color-coded images and spectra are the result of k-means cluster analysis of a 20 μm × 20 μm large raster image area encompassing a single cell. Figure 5b presents the result of cluster analysis of a 5 μm × 5 μm large area, a close-up of the MoO$_x$-BAB-M75 conjugate in a focal plane of Z = 3 μm. The individual data plots correspond to intensities of averaged spectra over each pixel per cluster, determined based on the pixels' spectral similarity. The individual cell compartments (intracellular matrix, nucleus and nucleolus, organelles, lipoprotein aggregates, membrane), the bioconjugates, and the extracellular matrix have a unique Raman signal that allows their differentiation. We analyze the so-called fingerprint region from 600 to 1800 rel. cm^{-1} together with the complementary high-frequency region from 2700 to 3800 rel. cm^{-1}. In our previous work, the positions of the individual molecular vibrations were described in detail, see Štefík et al.[85] Briefly, organelles, opposite the intracellular matrix, are characterized by an inverse intensity ratio between the peaks at 1582 (pyrimidine ring vibrational mode of adenine and guanine) and 1653 rel. cm^{-1} (amide I vibration in proteins and the lipid C=C stretching mode). In addition, the tryptophan ring breathing mode was at 742 rel. cm^{-1} is present. The nucleus can be characterized by a unique peak shape in the high-frequency region compared to those of other cell parts. The extracellular space, in our case PBS, obviously lacks the biochemical molecules fingerprint but demonstrates the O−H bending (1635 rel. cm^{-1}) and the symmetric and asymmetric O−H stretching (3248 rel. cm^{-1}, 3388 rel. cm^{-1}) modes of
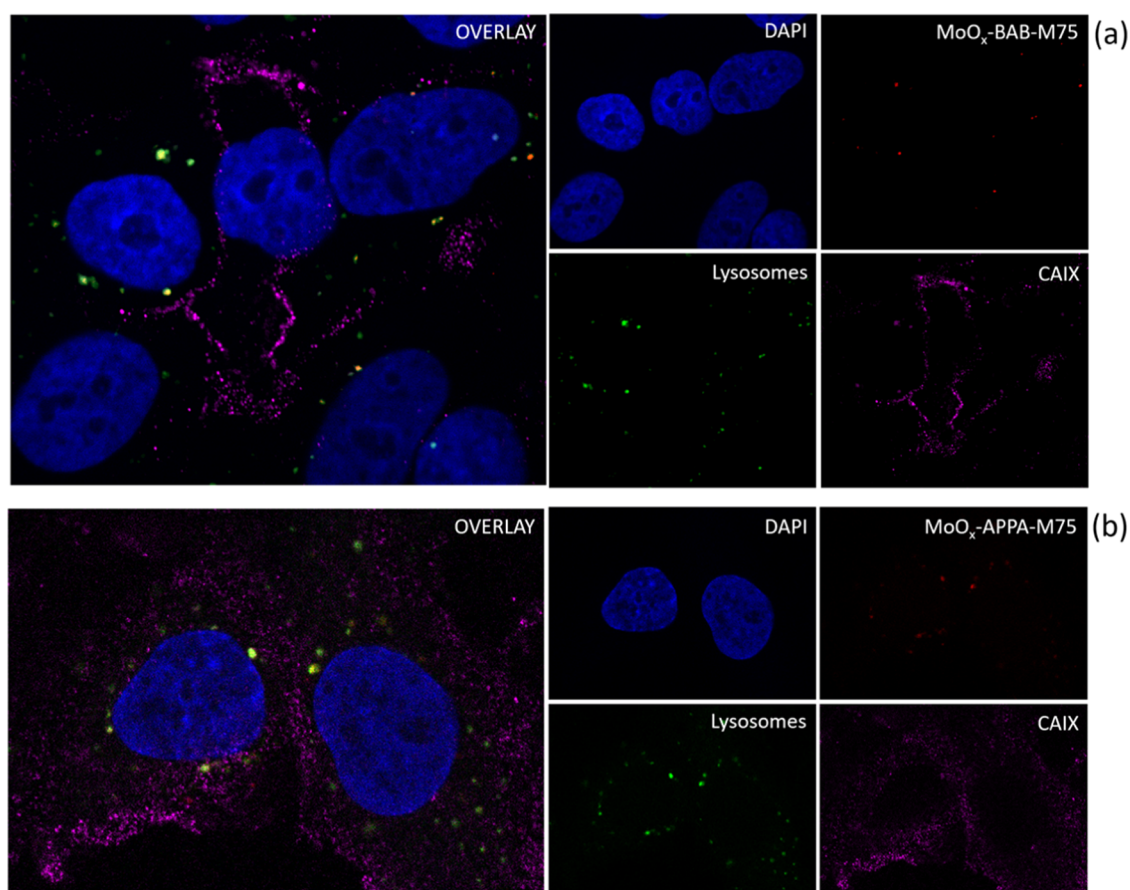
Figure 6. STED fluorescent imaging of cellular uptake and colocalization of MoO$_x$-BAB-M75 (a) and MoO$_x$-APPA-M75 (b) nanoconjugates after 24 h of incubation with the A549 cell line. Blue fluorescence corresponds to DAPI dye denoting the nucleus, red to Abberior STAR RED denoting the conjugate, green to LysoTracker Red denoting lysosomes, and magenta to Alexa Fluor 488 denoting CAIX on the cells membrane. Image sizes are 56 μm × 49 μm with pixel size of 50 nm and 54 μm × 39 μm with pixel size of 100 nm, for (a) and (b), respectively.

water. The MoO$_x$ bioconjugates were identified based on the presence of multiple MoO$_x$ peaks between 100 and 800 rel. cm^{-1}. For comparison, we provide in the Supporting Information the Raman spectrum of MoO$_x$ nanoparticles drop-cast on a germanium wafer (Figure S14). Cluster analysis of the nanoconjugates close-up scan resulted in the differentiation of the conjugate and the space around the conjugate into different regions, all of which contained MoO$_x$ peaks, see Figure 5b. It should be noted that, in our experience, the emerging weak fluorescence (light gray curve) often occurs around imaged nanoconjugates. The Raman peak positions correspond more or less to the tabulated MoO$_3$ Raman peaks according to refs 41,87−89. The observed oxygen vacancies can be responsible for the shifts in Raman peak positions, as well as the binding events with the linkers and antibodies.

By scanning the cell volume, we can build a 3D image of a single cell and observe the progressive appearance and disappearance of the internalized nanoconjugates. Figure 5 shows the false-color images obtained from scans at multiple focal planes of a JIMT-1 cell with a 2 μm step size. The MoO$_x$-BAB-M75 nanoconjugate was localized at $Z = 0$, -2, and -4 μm. With regard to the spatial and in-depth resolution of the CRM method, being about 650 nm and 1 μm, respectively, an approximate size of 1 μm × 4 μm can be attributed to the localized conjugates. These dimensions are considerably larger than the conjugate size determined by AFM measurements (around 10−20 nm in diameter). However, the conjugates

identified by this method can only be those that are already composed of several binding sites with CAIX in larger cell compartments after their transport through the membrane and intracellular space. Although CRM cannot compete with high-resolution fluorescence microscopes, it allows for the monitoring of live cells and the identification of different cell structures in a single scan.

Further examples of CRM-imaged cells incubated for 24 h with MoO$_x$-M75 nanoconjugates prepared using amino-phosphonic acid linkers are presented in Figure 5d. MoO$_x$-APPA-M75 conjugates localized in BxPC3 and A549 cell lines are shown as (i) and (ii), respectively. In addition, (iii) shows the MoO$_x$-ABPA-M75 conjugate localized in C33 CAIX. Note that all conjugates were found to be surrounded by endolysosomal system structures, identified here as organelles. These results are consistent with our previous findings that M75 antibody conjugated nanoplatforms are preferentially transported to organelles after 24 h of incubation.[9] Nevertheless, in the case of the MoO$_x$-M75 conjugates, we observed a relatively lower number of cells exhibiting lipoprotein aggregates compared with MoS$_2$- or graphene oxide-based M75 conjugates.[10,85] An example of such structures can be seen in (ii) in Figure 5d, marked by orange color. The corresponding Raman spectra are shown in Figure S15. The signal of lipids can be characterized by the presence of intense peaks at 1438 and 1655 rel.cm^{-1}, as well as at 2845 and 2880 rel.cm^{-1}.[81,90]

Finally, the label-free CRM technique was also applied to C33 neo cell lines after incubation with different conjugate types. In these cases, no conjugate was identified in either the intracellular or extracellular spaces. This is consistent with flow cytometry results showing very low binding in the absence of CAIX on the cell membrane.

Using fluorescent labels and a novel STED (stimulated emission depletion) setup, we could image the nanoconjugates in fixed cells with high spatial resolution. Figure 6a,b shows the internalized MoO_x-BAB-M75 and MoO_x-APPA-M75 conjugates in A549 cells, respectively. Nanoconjugates are shown with red staining, the distribution of CAIX on the cell membrane with magenta, while lysosomes are colored green. In the image with overlays of all color channels, spots with a yellowish-orange signal are visible. This indicates the colocalization of nanoparticles with lysosomes, a finding consistent with the live cell CRM analysis. In addition, we highlight the unique visualization of the CAIX antigens distribution on the cell membrane (magenta).

The STED results are complemented by standard CLSM imaging. A comparison of the internalization between C33 CAIX and C33 neo cells after 24 h of incubation with the MoO_x-ABPA-M75 conjugate is shown in Figure S16a and S16b, respectively. The positive signal corresponding to the labeled conjugates is evidently higher in CAIX-expressing cells, confirming the antibody-directed delivery of MoO_x-M75 conjugates through the CAIX protein located on the cell surface. Figure S17 presents further examples of cellular uptake of MoO_x-M75 conjugates in the case of different cell lines, A549, HCT116, and C33 CAIX.

■ CONCLUSIONS

Molybdenum oxides represent emerging 2D plasmonic nanomaterials with robust and scalable photothermal properties and attractive pH-dependent activity. Although MoO_x is still new, there is already a considerable amount of in vitro and in vivo work focused on developing anticancer photothermal therapy agents based on this type of nanomaterial. The present work fills the gap in the current literature by exploring MoO_x-based photothermal nanoconjugates as active targeting platforms.

MoO_x nanoparticles with a 3.7 ± 1.5 nm lateral size were prepared by a simple liquid-phase exfoliation technique. They were further conjugated with monoclonal antibodies M75. M75 is known to bind highly specific to carbonic anhydrase IX (CAIX) antigen, present on the cancer cell surface under hypoxic conditions. This is an original approach to selectively deliver MoO_x-based photoagents to the tumor site. We studied two conjugation schemes employing either small aminophosphonic acid linkers, APPA and ABPA, or a PEG chain combined with a biotin−avidin−biotin bridge. The selective tumor-targeting nature of MoO_x-M75 nanoconjugates, under in vitro conditions, was more prevailing in the case of the APPA and ABPA aminophosphonic acid molecules. Therefore, our study promotes the use of small organophosphonic linkers for bioconjugation purposes.

The morphological, physical, and chemical properties of the nanoparticles and nanoconjugates were thoroughly characterized in this present study. The conjugation success was confirmed by studying the changes of water molecules in near-IR spectrum (aquaphotomics), together with FTIR and XPS. The conjugation of the MoO_x nanoparticles with M75 antibody did not cause a significant change in the optical and photothermal properties of the final bioconjugates. Our

present work also confirmed the pH-dependent behavior of MoO_x, as reported by previous studies.

Cellular uptake of the MoO_x-M75 bioconjugates was monitored in addition to flow cytometry and fluorescence microscopy by less conventional label-free live cell confocal Raman microscopy and stimulated emission depletion nanoscopy. Both the label-free and fluorescently labeled localization techniques consistently indicated that conjugates are preferentially internalized in lysosome-rich regions. Standard cancer cell line monolayers with endogenous CAIX expression, and a model cell line C33 artificially expressing CAIX on the cell membrane (C33 CAIX) with a negative control cell group (C33 neo) were employed. In the C33 CAIX cells, the aminophosphonic acid linker-based schemes showed high positivity ranging from 55 up to 79% of positive cells binding MoO_x-M75 nanoconjugates, while in the case of the PEG and biotin−avidin−biotin bridge-based scheme, only around 12% was reached. The aminophosphonic acid linker-based conjugates also showed significantly increased binding efficiencies over the PEG-based one, in the case of A549 and JIMT-1 cells, where positivity reached around 82 and 57% of cells, respectively. In C33 neo, the binding does not exceed 5%, thus validating the highly selective nature of the bioconjugate delivery through M75-CAIX binding.

Molybdenum oxides present an intriguing alternative to standard noble-metal-based photoagents, such as gold-based nanostructures currently known for their powerful plasmonic heating performances. As a 2D nanomaterial, MoO_x displays a surface-to-volume ratio more favorable than that of gold nanoparticles and thus provides more functionalization opportunities for targeted delivery and bioimaging. Furthermore, unlike gold nanospheres, they do not suffer from such a high degree of clustering. The MoO_x nanoparticles prepared in this work show very good water solubility and high colloidal stability with a ζ potential as low as -50 mV. Moreover, we have shown that MoO_x-M75 conjugates combined with selective drug-free targeting are encouraging mediators for photothermal therapy. In addition, the pH-dependent functionality, coupled to selective targeting properties, can be exploited for advanced cancer therapy in the future.

■ EXPERIMENTAL SECTION

Nanoparticle Characterization. The morphology and crystalline structure of the samples were characterized using a JEOL JEM ARM200CF high-resolution transmission electron microscope (HRTEM) equipped with an image corrector operated at 80 and 200 kV. The nanoparticles from the solution were dispersed on a copper mesh grid covered with an amorphous carbon layer. The images were recorded with a Gatan UltraScan CCD camera (2k × 2k) and a Gatan Orius Model 830 SC200 CCD camera (2k × 2k).

AFM measurements were performed using a Bruker MultiMode 8. Samples were prepared following a simple mixing step with ethanol to ensure the best particle dispersion on the planar substrate and its subsequent imaging. 40 μL of MoO_x or MoO_x-M75 solutions was mixed with 2000 μL of ethanol, then 20 μL of this mixture was dropped onto a precleaned silicon wafer.

Grazing-incidence XRD (GIXRD) in coplanar geometry (diffractometer setup D8 Discover SSS with rotating anode, Bruker AXS) was performed with Cu Kα radiation at 40 kV/ 300 mA exposure and a fixed incident angle of 1°.

XPS measurements were recorded using a NEXSA-G2 system (Thermo Fisher Scientific, U.K.) equipped with a microfocused, monochromatic Al Kα X-ray source (1486.68 eV). An X-ray beam was focused on a 400 μm spot on the sample surface. The samples were prepared by gradually dropping about 1 mL of solution on a precleaned silicon wafer (the same preparation process was used in the case of GIXRD measurements). The spectra for the survey were acquired in constant analyzer energy mode with a pass energy of 200 eV. The high-resolution spectra were collected with a pass energy of 50 eV. Charge compensation was achieved with an Ar flood gun system. The Thermo Scientific Avantage software (version 6.5, Thermo Fisher Scientific) was used for digital acquisition and data processing.

The electronic properties of MoO_x were studied by electron paramagnetic resonance (EPR) at ambient temperature using a Varian E-line E-4 EPR spectrometer system (Varian Medical Group), operating at a frequency of 9.295 GHz.

The ζ potential measurements were performed using a Malvern Zetasizer Nano ZS90.

Near-IR spectral data acquisition in the wavenumber range 4450−9430 cm^{-1} was performed on a BW Tek detector (Sol. 2.2) with an integration time of 1000 μs, using a BPS 2.0 light source and optical fiber cables of a diameter 100 μm connected to a fiber-coupled cuvette holder BW Tek.

Fourier Transform IR (FTIR) spectroscopy was performed on a Vertex 80v (Bruker, Billerica, MA) instrument with a KBr beam splitter in transmission mode. Transmittance was measured in the wavenumber range of 3500−450 cm^{-1} (mid-infrared region), as an average value of the 64 scans per sample with 4 cm^{-1} resolution. Spectra were measured from dried films gradually drop-cast from solution on ZnSe optical plates.

Absorbance measurements in the range of 300−1350 nm were realized by a SolidSpec-3700 UV−vis−NIR spectrophotometer (Shimadzu, Japan) using an integrating sphere. Deionized water or a 45% ethanol/water solution was used for baseline correction prior to measurements and also as a reference sample during measurements.

The photothermal properties were studied by temperature measurements upon laser irradiation of the colloidal samples by using a K-type thermocouple coupled to an Extech SDL200 data-logging thermometer. For the measurements, a volume of 100 μL we tested. The excitation source was an 808 nm laser diode module with a power of 350 mW and a power density of 0.55 W cm^{-2}. The laser beam diameter was expanded to illuminate a cell with a 6.4 mm diameter and 10 mm depth. The sonde was placed inside the cell and immersed in the nanoparticle solution. In the case of the measurements of dried MoO_x nanoparticle powder, the material was placed in the quartz capillary tube used for the EPR measurements. In this case, laser light was transmitted through the quartz tube. The sonde was placed in contact with the outer side of the quartz tube.

The experiment on the nanoparticle stability as a function of pH was performed using an approximate volume of 150 mL of MoO_x aqueous colloidal solution (1−1.5 mg mL^{-1}). The pH was controlled by adding HCl and KOH and measured with a calibrated pH meter HANNA HI 5221-02 (Hanna Instruments). The pH was remeasured after 21 days using pH dip sticks (resolution 0.5).

CRM of pristine MoO_x nanoparticles dried on a Ge wafer was analyzed using a WITec Alpha300 R+ (Ulm, Germany)

confocal Raman microscope, coupled to a spectrometer (UHTS 300, WITec, Ulm, Germany), equipped with an 1800 gr/mm grating (blazed at 500 nm) and an EMCCD camera (Newton DU970N-BV-353, Andor, Belfast, U.K.). An excitation wavelength of 532 nm with a power of 125 μW, a 50×/0.8 Epiplan Neofluar (Zeiss, Germany) objective, and 100 μm diameter optical fiber were used. An area of 10 μm × 10 μm was scanned.

***In Vitro* Studies.** For *in vitro* studies, we have used the lung cancer cell line A549 (CCL-185, ATCC); pancreatic adenocarcinoma cell line BxPC3 (CRL-1687, ATCC); and pancreatic adenosquamous carcinoma cell line COLO357 (RRID: CVCL 0221); pharynx squamous carcinoma cell line FaDu (HTB-34, ATCC); colorectal carcinoma cell line HCT116 (CCL-247, ATCC); and breast carcinoma cell line JIMT-1 (ACC 589, DSMZ, Germany). The original C33 A cell line (HTB-31, ATCC) was derived from human cervix carcinoma. C33 A cell line was stably transfected with pSG5c-MN/CA9 ([91]GenBank No. X66839, full-length cDNA of Carbonic anhydrase IX), designated as C33 CAIX and empty control pSG5c vector (pSG5c-mock, Stratagene, Cedar Creek), designated as C33 neo.[74]

All cell lines were routinely cultivated in DMEM medium (Lonza, Basel, Switzerland) supplemented with 10% bovine fetal serum (Lonza, Basel, Switzerland) in humidified CO_2 atmosphere in a thermostat at 37 °C. For experiments, the cells were incubated for 48 h in a hypoxia workstation (Ruskinn Technologies, Bridgend, U.K.) with 1% O_2 (5% CO_2, 10% H_2, and 83% N_2) atmosphere to induce CAIX protein levels.

The cell viability was measured by a Cell titer blue viability assay kit (Promega, San Luis) according to the manufacturer's instructions. The cells were seeded in a concentration of 10.000 cells per well in a 96-well plate and incubated for 24 h at 37 °C in 5% CO_2 atmosphere. The 40 μL of nanoparticle or nanoconjugates solutions (at a concentration of 3 mg mL^{-1}), were added to 100 μL of media (i.e., 120 μg/well, 0.86 mg mL^{-1}). After 24 h of incubation at 37 °C, 20 μL of Cell titer blue reagent was added. The cells were further incubated for 1 h, and absorbance values at the wavelength of 590 nm were measured (Synergy HT reader, BioTek).

Flow cytometry was used to analyze and quantify the number of cells with fluorescently labeled functionalized nanoparticles bound to the membrane or localized inside the cells. The nanoparticles functionalized with the M75 antibody, specifically recognizing CAIX, attach to the membrane. The cells were seeded on a 96-well plate at a concentration of 10,000 cells per well. The cells were left to attach until the next day and then introduced into the hypoxia workstation with a 1% O_2 atmosphere for 48 h. After 48 h, the nanoparticle solutions were incubated with a secondary antibody anti-mouse Alexa Fluor 488 conjugated antibody (Invitrogen, CA, Exc/Em peak 499/520) in a dilution ratio of 1:1000 and incubated for 1 h at 37 °C on a rotation shaker. After incubation, 40 μL of nanoparticle or nanoconjugates solutions (at a concentration of 3 mg mL^{-1}) were added into 100 μL of medium (i.e. 120 μg/well, 0.86 mg mL^{-1}) inside the hypoxic workstation and incubated for 24 h. Then, the cells were trypsinized and the cell suspension was resuspended in PBS with 10% FCS and centrifuged at 800 rpm for 5 min at 4 °C. PBS washed cells were analyzed in the flow cytometer (Guava EasyCyte Plus instrument, Merck, Darmstadt, Germany). The results were processed in CytoSoft Software and Excel software. The cells without nanoparticles, cells with non-

functionalized nanoparticles, and cells with secondary antibody-AF488 unlabeled nanoparticles were used as controls. Each experiment was done in quadruplicate, and statistical analysis was determined. The average value of the percentage of positive cells, the standard deviation, and Student's t test were evaluated. $P < 0.05$ was assumed to be significant (*$P <$ 0.05, **$P < 00.01$, ***$P < 0.005$).

The cells for Western blot were seeded at a concentration of 500,000 cells pre 3.5 cm Petri dish and incubated for 48 h in hypoxia workstation at 1% O_2. Confluent monolayers were rinsed with PBS and collected in RIPA lysis buffer (50 mM Tris−HCl pH 7.4; 150 mM NaCl, 1% Triton X-100; 5% deoxycholate; 1 mM EDTA, 0.1% SDS; protease inhibitors). The extracts were cleared by centrifugation at 13,000 rpm for 15 min at 4 °C, and the total proteins were measured with Pierce BCA protein assay kit (Thermo Fisher). 25 μg of total proteins was loaded onto 10% PAGE. Proteins were transferred onto the PVDF membrane (Immobilon-P, Millipore), and the membrane was blocked for 1 h in 5% milk with 0.2% Nonidet 40. Primary antibodies, M75 hybridoma medium[15] diluted medium 1:3 in milk and anti-β-actin antibody diluted in 1% BSA with 0.2% Nonidet 40 (Cell Signaling, WB: 1:5000) and incubated for 1 h. The membrane was washed three times for 10 min with PBS supplemented with 0.2% Nonidet 40. The secondary anti-mouse antibody labeled with horseradish peroxidase (polyclonal goat anti-mouse immunoglobulins conjugated with horseradish peroxidase, diluted 1:5000, Dako, Glostrup, Denmark) was diluted in 1% BSA with 0.2% Nonidet 40 and again incubated for 1 h. After the cells were washed, protein bands were visualized by enhanced chemiluminescence using the ECL kit (GE Healthcare Bio-Sciences).

The cells for CRM were seeded at a concentration of 300,000 cells per well in a 6-well plate with coverslips. The cells were cultivated until the next day and transferred to the hypoxia workstation for at least 48 h. After 48 h, for 3 mL of media, 280 μL of nanoparticles was added inside the hypoxia workstation and incubated for another 24 h. Label-free CRM (Alpha300 R+, WITec, Ulm, Germany) was applied to living cells on glass coverslips immersed in PBS (pH 7.4, Oxoid, Basingstoke, U.K.). The cell monolayers were first gently washed three times in PBS. We used an immersive W Plan-Apochromat 63×/1 objective (Zeiss, Germany). The samples were excited at wavelengths and powers of 532 nm and 5 mW, respectively (Spectra-Physics Excelsior 532-60 Multi Mode). The Raman spectra were acquired through a 50 μm diameter multimode optical fiber, also acting as a pinhole providing confocality, into a spectrometer (UHTS 300, WITec, Ulm, Germany) equipped with a 600 gr/mm grating (blazed at 500 nm), coupled to an EMCCD camera (Newton DU970N-BV-353, Andor, Belfast, U.K.). Areas of 20 μm × 20 μm were scanned by raster imaging of single cells at multiple focal planes. The step size was 200 nm (in both horizontal and vertical directions), and the integration time was 100 ms. The total acquisition time for one scan per cell was 20 min. The lateral and vertical spatial resolutions are about 650 nm and 1 μm, respectively.

The cells for confocal laser scanning microscopy (CLSM) and STED were prepared on coverslips according to the protocol used for CRM. However, the nanoparticles were labeled with secondary antibody anti-mouse Alexa Fluor 488 conjugated antibody (Invitrogen, CA, Exc/Em peak 499/520) and goat anti-mouse Star Red-conjugated antibody (also

known as KK114, Abberior, Exc/Em peak 638/655, STED depletion min/max 750/800), in the case of CLSM and STED, respectively. Before fixation, LysoTracker Red (Life Technologies, Paisley, U.K., Exc/Em peak 577/590) was added to the cells, and the cells were incubated for 30 min. While CAIX, in the case of STED measurements, was labeled with Alexa Fluor 488 conjugated M75 (Invitrogen, CA, Exc/Em peak 499/520). The coverslips were washed and fixed with 4% paraformaldehyde for 20 min at room temperature and washed with PBS. The coverslips were mounted with Fluoroshield mounting media containing DAPI (Abcam, Cambridge, U.K.). The samples were analyzed and images were acquired using a Zeiss LSM510 laser scanning confocal microscopy system mounted on a Zeiss Axiovert 200 M inverted microscope and an Abberior STEDYCON STED super-resolution microscope using Plan Apochromat 63×/1.4 oil and 100×/1.4 oil objectives, respectively.

For immunofluorescent analysis of CAIX expression and localization, CAIX was detected by M75 primary antibody,[15] and subsequently stained by Alexa Fluor 488 conjugated anti-mouse secondary antibody (Invitrogen, CA, Exc/Em peak 499/520). The samples were further processed (see above the coverslip preparation) and imaged by CLSM using a Zeiss LSM510.

■ ASSOCIATED CONTENT

Ⓢ Supporting Information

The Supporting Information is available free of charge at https://pubs.acs.org/doi/10.1021/acsomega.3c01934.

> Experimental details concerning nanoparticle synthesis and bioconjugation with M75 antibodies; examples of AFM images with line profiles for the conjugates; GIXRD pattern from pristine MoO_x nanoparticles and MoO_2 microcrystalline powder; XPS results on the Mo 3d region; near IR spectra of water for MoO_x conjugates and related control solutions (aquaphotomics); FTIR spectra of MoO_x conjugates; apparent surface chemical composition as determined by XPS; change in the absorbance of pristine MoO_x nanoparticles as a function of pH; controls for flow cytometry results; additional CRM and CLSM results (PDF)

■ AUTHOR INFORMATION

Corresponding Author

Adriana Annušová − *Institute of Physics, Slovak Academy of Sciences, 845 11 Bratislava, Slovakia; Centre for Advanced Materials Application, Slovak Academy of Sciences, 845 11 Bratislava, Slovakia;* ⓞ orcid.org/0000-0002-3769-9287; Email: adriana.annusova@savba.sk

Authors

Martina Labudová − *Centre for Advanced Materials Application, Slovak Academy of Sciences, 845 11 Bratislava, Slovakia; Institute of Virology, Biomedical Research Center, Slovak Academy of Sciences, 845 05 Bratislava, Slovakia; Faculty of Natural Sciences, Comenius University in Bratislava, 842 15 Bratislava, Slovakia*

Daniel Truchan − *Institute of Physics, Slovak Academy of Sciences, 845 11 Bratislava, Slovakia; Université Sorbonne Paris Nord, Université Paris Cité, Laboratory for Vascular Translational Science, LVTS, INSERM, UMR 1148, Bobigny F-93017, France*

Veronika Hegedűšová − *Institute of Physics, Slovak Academy of Sciences, 845 11 Bratislava, Slovakia; Faculty of Natural Sciences, Comenius University in Bratislava, 842 15 Bratislava, Slovakia*

Helena Švajdlenková − *Faculty of Natural Sciences, Comenius University in Bratislava, 842 15 Bratislava, Slovakia; Polymer Institute, Slovak Academy of Sciences, 845 41 Bratislava, Slovakia;* orcid.org/0000-0002-6439-6417

Matej Mičušík − *Polymer Institute, Slovak Academy of Sciences, 845 41 Bratislava, Slovakia*

Mário Kotlár − *Centre for Nanodiagnostics of Materials, Slovak University of Technology in Bratislava, 812 43 Bratislava, Slovakia*

Lenka Pribusová Slušná − *Centre for Advanced Materials Application, Slovak Academy of Sciences, 845 11 Bratislava, Slovakia; Institute of Electrical Engineering, Slovak Academy of Sciences, 841 04 Bratislava, Slovakia;* orcid.org/0000-0002-4653-4492

Martin Hulman − *Institute of Electrical Engineering, Slovak Academy of Sciences, 841 04 Bratislava, Slovakia;* orcid.org/0000-0002-5598-9245

Farnoush Salehtash − *Institute of Physics, Slovak Academy of Sciences, 845 11 Bratislava, Slovakia*

Anna Kálosi − *Institute of Physics, Slovak Academy of Sciences, 845 11 Bratislava, Slovakia; Centre for Advanced Materials Application, Slovak Academy of Sciences, 845 11 Bratislava, Slovakia*

Lucia Csáderová − *Centre for Advanced Materials Application, Slovak Academy of Sciences, 845 11 Bratislava, Slovakia; Institute of Virology, Biomedical Research Center, Slovak Academy of Sciences, 845 05 Bratislava, Slovakia*

Eliška Švastová − *Centre for Advanced Materials Application, Slovak Academy of Sciences, 845 11 Bratislava, Slovakia; Institute of Virology, Biomedical Research Center, Slovak Academy of Sciences, 845 05 Bratislava, Slovakia*

Peter Šiffalovič − *Institute of Physics, Slovak Academy of Sciences, 845 11 Bratislava, Slovakia; Centre for Advanced Materials Application, Slovak Academy of Sciences, 845 11 Bratislava, Slovakia*

Matej Jergel − *Institute of Physics, Slovak Academy of Sciences, 845 11 Bratislava, Slovakia; Centre for Advanced Materials Application, Slovak Academy of Sciences, 845 11 Bratislava, Slovakia;* orcid.org/0000-0002-4482-7881

Silvia Pastoreková − *Institute of Virology, Biomedical Research Center, Slovak Academy of Sciences, 845 05 Bratislava, Slovakia*

Eva Majková − *Institute of Physics, Slovak Academy of Sciences, 845 11 Bratislava, Slovakia; Centre for Advanced Materials Application, Slovak Academy of Sciences, 845 11 Bratislava, Slovakia;* orcid.org/0000-0001-9597-9247

Complete contact information is available at:
https://pubs.acs.org/10.1021/acsomega.3c01934

Author Contributions

A.A.: Conceptualization, investigation, writing—original draft, writing—review & editing, visualization, project administration, funding acquisition; M.L.: Investigation, writing—original draft; D.T.: Investigation; V.H.: Investigation; H.Š.: Investigation, writing—original draft; M.M.: Investigation, writing—original draft; M.K.: Investigation; L.P.S.: Investigation; M.H.: Resources; F.S.: Investigation; A.K.: Investigation, writing—review & editing; L.C.: Investigation, writing— review & editing, project administration, funding acquisition; E.Š.: Writing—review & editing, supervision, funding acquisition; P.Š.: Writing—review & editing, supervision, project administration; M.J.: Writing—review & editing, supervision, funding acquisition; S.P.: Supervision, funding acquisition; E.M.: Writing—review & editing, supervision, project administration, funding acquisition.

Notes

The authors declare no competing financial interest.

■ REFERENCES

(1) Tian, H.; Zhang, T.; Qin, S.; Huang, Z.; Zhou, L.; Shi, J.; et al. Enhancing the therapeutic efficacy of nanoparticles for cancer treatment using versatile targeted strategies. *J. Hematol. Oncol.* **2022**, *15* (1), No. 132.

(2) Dutta, B.; Barick, K. C.; Hassan, P. A. Recent advances in active targeting of nanomaterials for anticancer drug delivery. *Adv. Colloid Interface Sci.* **2021**, *296*, No. 102509.

(3) Thang, D. C.; Wang, Z.; Lu, X.; Xing, B. Precise cell behaviors manipulation through light-responsive nano-regulators: recent advance and perspective. *Theranostics* **2019**, *9* (11), 3308.

(4) Engin, A. B.; Nikitovic, D.; Neagu, M.; Henrich-Noack, P.; Docea, A. O.; Shtilman, M. I.; et al. Mechanistic understanding of nanoparticles' interactions with extracellular matrix: the cell and immune system. *Part. Fibre Toxicol.* **2017**, *14* (1), No. 22.

(5) Liu, X. Q.; Tang, R. Z. Biological responses to nanomaterials: understanding nano-bio effects on cell behaviors Biological responses to nanomaterials: understanding nano-bio effects on cell behaviors. *Drug Delivery* **2017**, *24* (2), 1−15.

(6) Mitchell, M. J.; Billingsley, M. M.; Haley, R. M.; Wechsler, M. E.; Peppas, N. A.; Langer, R. Engineering precision nanoparticles for drug delivery. *Nat. Rev. Drug Discovery* **2021**, *20* (2), 101−124.

(7) Yao, Y.; Zhou, Y.; Liu, L.; Xu, Y.; Chen, Q.; Wang, Y.; et al. Nanoparticle-Based Drug Delivery in Cancer Therapy and Its Role in Overcoming Drug Resistance. *Front. Mol. Biosci.* **2020**, *7*, No. 193.

(8) Maeda, H.; Nakamura, H.; Fang, J. The EPR effect for macromolecular drug delivery to solid tumors: Improvement of tumor uptake, lowering of systemic toxicity, and distinct tumor imaging in vivo. *Adv. Drug Delivery Rev.* **2013**, *65* (1), 71−79.

(9) Kálosi, A.; Labudová, M.; Annušová, A.; Benkovičová, M.; Bodík, M.; Kollár, J.; et al. A bioconjugated MoS_2 based nanoplatform with increased binding efficiency to cancer cells. *Biomater. Sci.* **2020**, *8* (7), 1973−1980.

(10) Bugárová, N.; Annušová, A.; Bodík, M.; Šiffalovič, P.; Labudová, M.; Kajanová, I.; et al. Molecular targeting of bioconjugated graphene oxide nanocarriers revealed at a cellular level using label-free Raman imaging. *Nanomedicine* 2020, *30*, No. 102280.

(11) Pastorekova, S.; Ratcliffe, P. J.; Pastorek, J. Molecular mechanisms of carbonic anhydrase IX-mediated pH regulation under hypoxia. *BJU Int.* 2008, *101*, 8–15.

(12) Ward, C.; Meehan, J.; Gray, M.; Kunkler, I. H.; Langdon, S. P.; Argyle, D. J. Carbonic Anhydrase IX (CAIX), Cancer, and Radiation Responsiveness. *Metabolites* 2018, *8* (1), No. 13, DOI: 10.3390/metabo8010013.

(13) Pastorek, J.; Pastorekova, S. Hypoxia-induced carbonic anhydrase IX as a target for cancer therapy: From biology to clinical use. *Semin. Cancer Biol.* 2015, *31*, 52–64.

(14) Rafajová, M.; Zatovicova, M.; Kettmann, R.; Pastorek, J.; Pastoreková, S. Induction by hypoxia combined with low glucose or low bicarbonate and high posttranslational stability upon reoxygenation contribute to carbonic anhydrase IX expression in cancer cells. *Int. J. Oncol.* 2004, *24* (4), 995–1004.

(15) Pastoreková, S.; Závadová, Z.; Košt'ál, M.; Babušíková, O.; Závada, J. A novel quasi-viral agent, MaTu, is a two-component system. *Virology* 1992, *187* (2), 620–626.

(16) Merkx, R. I. J.; Rijpkema, M.; Franssen, G. M.; Kip, A.; Smeets, B.; Morgenstern, A.; et al. Carbonic Anhydrase IX-Targeted α-Radionuclide Therapy with 225Ac Inhibits Tumor Growth in a Renal Cell Carcinoma Model. *Pharmaceuticals* 2022, *15* (5), 570.

(17) Chrastina, A.; Závada, J.; Parkkila, S.; Kaluz, Š.; Kaluzová, M.; Rajčáni, J.; et al. Biodistribution and pharmacokinetics of 125I-labeled monoclonal antibody M75 specific for carbonic anhydrase IX, an intrinsic marker of hypoxia, in nude mice xenografted with human colorectal carcinoma. *Int. J. Cancer* 2003, *105* (6), 873–881.

(18) Debreova, M.; Csaderova, L.; Burikova, M.; Lukacikova, L.; Kajanova, I.; Sedlakova, O.; et al. CAIX Regulates Invadopodia Formation through Both a pH-Dependent Mechanism and Interplay with Actin Regulatory Proteins. *Int. J. Mol. Sci.* 2019, *20* (11), 2745.

(19) Murri-Plesko, M. T.; Hulikova, A.; Oosterwijk, E.; Scott, A. M.; Zortea, A.; Harris, A. L.; et al. Antibody inhibiting enzymatic activity of tumour-associated carbonic anhydrase isoform IX. *Eur. J. Pharmacol.* 2011, *657* (1–3), 173–183.

(20) Takacova, M.; Kajanova, I.; Kolarcikova, M.; Lapinova, J.; Zatovicova, M.; Pastorekova, S. Understanding metabolic alterations and heterogeneity in cancer progression through validated immuno-detection of key molecular components: a case of carbonic anhydrase IX. *Cancer Metastasis Rev.* 2021, *40* (4), 1035–1053.

(21) Opavský, R.; Pastoreková, S.; Zelník, V.; Gibadulinová, A.; Stanbridge, E. J.; Závada, J.; et al. Human MN/CA9 gene, a novel member of the carbonic anhydrase family: Structure and exon to protein domain relationships. *Genomics* 1996, *33* (3), 480–487.

(22) Ma, H.; Xue, M. Recent advances in the photothermal applications of two-dimensional nanomaterials: photothermal therapy and beyond. *J. Mater. Chem. A* 2021, *9* (33), 17569–17591.

(23) Bian, W.; Wang, Y.; Pan, Z.; Chen, N.; Li, X.; Wong, W. L.; et al. Review of Functionalized Nanomaterials for Photothermal Therapy of Cancers. *ACS Appl. Nano Mater.* 2021, *4* (11), 11353–11385.

(24) Song, G.; Shen, J.; Jiang, F.; Hu, R.; Li, W.; An, L.; et al. Hydrophilic molybdenum oxide nanomaterials with controlled morphology and strong plasmonic absorption for photothermal ablation of cancer cells. *ACS Appl. Mater. Interfaces.* 2014, *6* (6), 3915–3922.

(25) Ding, D.; Guo, W.; Guo, C.; Sun, J.; Zheng, N.; Wang, F.; et al. MoO_{3-x} quantum dots for photoacoustic imaging guided photo-thermal/photodynamic cancer treatment. *Nanoscale* 2017, *9* (5), 2020–2029.

(26) Yang, H.; Guo, Y.; Zhuang, Z.; Zhong, H.; Hu, C.; Liu, Z.; Guo, Z. Molybdenum oxide nano-dumplings with excellent stability for photothermal cancer therapy and as a controlled release hydrogel. *New J. Chem.* 2019, *43* (36), 14281–14290.

(27) Li, N.; Li, Y.; Sun, G.; Zhou, Y.; Ji, S.; Yao, H.; et al. Enhanced photochromic modulation efficiency: A novel plasmonic molybdenum oxide hybrid. *Nanoscale.* 2017, *9* (24), 8298–8304.

(28) Liu, Q.; Wu, Y.; Zhang, J.; Chen, K.; Huang, C.; Chen, H.; Qiu, X. Plasmonic MoO_{3-x} nanosheets with tunable oxygen vacancies as efficient visible light responsive photocatalyst. *Appl. Surf. Sci.* 2019, *490*, 395–402.

(29) Etman, A. S.; Wang, L.; Edström, K.; Nyholm, L.; Sun, J. Molybdenum Oxide Nanosheets with Tunable Plasmonic Resonance: Aqueous Exfoliation Synthesis and Charge Storage Applications. *Adv. Funct. Mater.* 2019, *29* (4), No. 1806699.

(30) Datta, R. S.; Haque, F.; Mohiuddin, M.; Carey, B. J.; Syed, N.; Zavabeti, A.; et al. Highly active two dimensional α-MoO3-: X for the electrocatalytic hydrogen evolution reaction. *J. Mater. Chem. A* 2017, *5* (46), 24223–24231.

(31) Annušová, A.; Bodik, M.; Hagara, J.; Kotlár, M.; Halahovets, Y.; Micusik, M.; et al. On the extraction of MoO_x photothermally active nanoparticles by gel filtration from a byproduct of few-layer MoS_2 exfoliation. *Nanotechnology* 2021, *32*, No. 045708.

(32) Bodík, M.; Annušová, A.; Hagara, J.; Mičušík, M.; Omastová, M.; Kotlár, M.; et al. An elevated concentration of MoS_2 lowers the efficacy of liquid-phase exfoliation and triggers the production of MoO_x nanoparticles. *Phys. Chem. Chem. Phys.* 2019, *21* (23), 12396–12405.

(33) Huang, Q.; Hu, S.; Zhuang, J.; Wang, X. MoO3−x-Based Hybrids with Tunable Localized Surface Plasmon Resonances: Chemical Oxidation Driving Transformation from Ultrathin Nano-sheets to Nanotubes. *Chem. - Eur. J.* 2012, *18* (48), 15283–15287.

(34) Bao, T.; Yin, W.; Zheng, X.; Zhang, X.; Yu, J.; Dong, X.; et al. One-pot synthesis of PEGylated plasmonic MoO3−x hollow nanospheres for photoacoustic imaging guided chemo-photothermal combinational therapy of cancer. *Biomaterials* 2016, *76*, 11–24.

(35) Song, G.; Hao, J.; Liang, C.; Liu, T.; Gao, M.; Cheng, L.; et al. Degradable Molybdenum Oxide Nanosheets with Rapid Clearance and Efficient Tumor Homing Capabilities as a Therapeutic Nano-platform. *Angew. Chem., Int. Ed.* 2016, *55* (6), 2122–2126.

(36) Qi, X.; Peng, J.; Tang, D.; Wang, N.; Zou, H. PEGMa modified molybdenum oxide as a NIR photothermal agent for composite thermal/pH-responsive p(NIPAM-: Co -MAA) microgels. *J. Mater. Chem. C* 2017, *5* (34), 8788–8795.

(37) Yin, W.; Bao, T.; Zhang, X.; Gao, Q.; Yu, J.; Dong, X.; et al. Biodegradable MoOx nanoparticles with efficient near-infrared photothermal and photodynamic synergetic cancer therapy at the second biological window. *Nanoscale* 2018, *10* (3), 1517–1531.

(38) Zou, H.; Tang, D.; Wang, N.; Jia, S.; Sun, Z.; Yang, X.; Peng, J. Polyethylene glycol−modified molybdenum oxide as NIR photo-thermal agent and its ablation ability for HeLa cells. *Colloid Polym. Sci.* 2019, *297* (2), 249–260.

(39) Odda, A. H.; Xu, Y.; Lin, J.; Wang, G.; Ullah, N.; Zeb, A.; et al. Plasmonic MoO_{3-x} nanoparticles incorporated in Prussian blue frameworks exhibit highly efficient dual photothermal/photodynamic therapy. *J. Mater. Chem. B* 2019, *7* (12), 2032–2042.

(40) Agrawal, A.; Johns, R. W.; Milliron, D. J. Control of Localized Surface Plasmon Resonances in Metal Oxide Nanocrystals. *Annu. Rev. Mater. Res.* 2017, *47*, 1–31.

(41) Alsaif, M. M. Y. A.; Latham, K.; Field, M. R.; Yao, D. D.; Medhekar, Nv.; Beane, G. A.; et al. Tunable plasmon resonances in two-dimensional molybdenum oxide nanoflakes. *Adv. Mater.* 2014, *26* (23), 3931–3937.

(42) de Castro, I. A.; Datta, R. S.; Ou, J. Z.; Castellanos-Gomez, A.; Castellanos-Gomez, A.; Sriram, S.; Daeneke, T. Molybdenum Oxides − From Fundamentals to Functionality. *Adv. Mater.* 2017, *29* (40), No. 1701619.

(43) Zhu, C.; Xu, Q.; Ji, L.; Ren, Y.; Fang, M. Room-temperature Synthesis of Amorphous Molybdenum Oxide Nanodots with Tunable Localized Surface Plasmon Resonances. *Chem. Asian J.* 2017, *12* (23), 2980–2984.

(44) Xing, Y.; Cai, Y.; Cheng, J.; Xu, X. Applications of molybdenum oxide nanomaterials in the synergistic diagnosis and treatment of tumor. *Appl. Nanosci.* **2020**, *10* (7), 2069−2083.

(45) Qiu, N.; Yang, X.; Zhang, Y.; Zhang, J.; Ji, J.; Zhang, Y.; et al. A molybdenum oxide-based degradable nanosheet for combined chemo-photothermal therapy to improve tumor immunosuppression and suppress distant tumors and lung metastases. *J. Nanobiotechnol.* **2021**, *19* (1), 428.

(46) O'shannessy, D. J.; Somers, E. B.; Wang, L. C.; Wang, H.; Hsu, R. Discovery of Dachshund 2 protein as a novel biomarker of poor prognosis in epithelial ovarian cancer. *J. Ovarian Res.* **2015**, *8*, No. 6.

(47) Canepa, P.; Gonella, G.; Pinto, G.; Grachev, V.; Canepa, M.; Cavalleri, O. Anchoring of Aminophosphonates on Titanium Oxide for Biomolecular Coupling. *J. Phys. Chem. C* **2019**, *123* (27), 16843−16850.

(48) Boissezon, R.; Muller, J.; Beaugeard, V.; Monge, S.; Robin, J. J. Organophosphonates as anchoring agents onto metal oxide-based materials: Synthesis and applications. *RSC Adv.* **2014**, *4* (67), 35690−35707.

(49) Wapner, K.; Stratmann, M.; Grundmeier, G. Structure and stability of adhesion promoting aminopropyl phosphonate layers at polymer/aluminium oxide interfaces. *Int. J. Adhes Adhes.* **2008**, *28* (1−2), 59−70.

(50) Zhang, J.; Yeromonahos, C.; Léonard, D.; Géhin, T.; Botella, C.; Grenet, G.; et al. Oxidized Titanium Tungsten Surface Functionalization by Silane-, Phosphonic Acid-, or Ortho-dihydrox-yaryl-Based Organolayers. *Langmuir* **2019**, *35* (29), 9554−9563.

(51) Silverman, B. M.; Wieghaus, K. A.; Schwartz, J. Comparative Properties of Siloxane vs Phosphonate Monolayers on A Key Titanium Alloy. *Langmuir* **2005**, *21* (1), 225−228.

(52) Wan, X.; Lieberman, I.; Asyuda, A.; Resch, S.; Seim, H.; Kirsch, P.; Zharnikov, M. Thermal Stability of Phosphonic Acid Self-Assembled Monolayers on Alumina Substrates. *J. Phys. Chem. C* **2020**, *124* (4), 2531−2542.

(53) Vega, A.; Thissen, P.; Chabal, Y. J. Environment-controlled tethering by aggregation and growth of phosphonic acid monolayers on silicon oxide. *Langmuir* **2012**, *28* (21), 8046−8051.

(54) Nie, H. Y. Self-assembled monolayers of octadecylphosphonic acid and polymer films: Surface chemistry and chemical structures studied by time-of-flight secondary ion mass spectrometry. *Surf. Interface Anal.* **2017**, *49* (13), 1431−1441.

(55) Dubey, M.; Gouzman, I.; Bernasek, S. L.; Schwartz, J. Characterization of self-assembled organic films using differential charging in X-ray photoelectron spectroscopy. *Langmuir* **2006**, *22* (10), 4649−4653.

(56) Thissen, P.; Valtiner, M.; Grundmeier, G. Stability of phosphonic acid self-assembled monolayers on amorphous and Single-crystalline aluminum oxide surfaces in aqueous solution. *Langmuir* **2010**, *26* (1), 156−164.

(57) Zhao, R.; Rupper, P.; Gaan, S. Recent development in phosphonic acid-based organic coatings on aluminum. *Coatings* **2017**, *7* (9), 133.

(58) Pujari, S. P.; Scheres, L.; Marcelis, A. T. M.; Zuilhof, H. Covalent surface modification of oxide surfaces. *Angew. Chem., Int. Ed.* **2014**, *53* (25), 6322−6356.

(59) He, L.; Zhao, Y.; Xing, L.; Liu, P.; Wang, Z.; Zhang, Y.; Liu, X. Preparation of Phosphonic Acid Functionalized Graphene Oxide-modified Aluminum Powder with Enhanced Anticorrosive Properties. *Appl. Surf. Sci.* **2017**, *411*, 235−239.

(60) Tudisco, C.; Oliveri, V.; Cantarella, M.; Vecchio, G.; Condorelli, G. G. Cyclodextrin anchoring on magnetic Fe 3O 4 nanoparticles modified with phosphonic linkers. *Eur. J. Inorg. Chem.* **2012**, *2012*, 5323−5331.

(61) Santosh, K. C.; Longo, R. C.; Addou, R.; Wallace, R. M.; Cho, K. Electronic properties of MoS2/MoOx interfaces: Implications in Tunnel Field Effect Transistors and Hole Contacts. *Sci. Rep.* **2016**, *6* (1), No. 33562.

(62) Cai, L.; McClellan, C. J.; Koh, A. L.; Li, H.; Yalon, E.; Pop, E.; Zheng, X. Rapid flame synthesis of atomically thin MoO3 down to

monolayer thickness for effective hole doping of WSe2. *Nano Lett.* **2017**, *17* (6), 3854−3861.

(63) Watson, R. B.; Ozkan, U. S. Spectroscopic and Structural Characterization of Low-Level Alkali Doping Effects on Mo/Silica−Titania Catalysts. *J. Phys. Chem. B* **2002**, *106* (27), 6930−6941.

(64) Tan, X.; Wang, L.; Cheng, C.; Yan, X.; Shen, B.; Zhang, J. Plasmonic MoO3-x@MoO3 nanosheets for highly sensitive SERS detection through nanoshell-isolated electromagnetic enhancement. *Chem. Commun.* **2016**, *52* (14), 2893−2896.

(65) Tsenkova, R.; Muncan, J.; Pollner, B.; Kovacs, Z. Essentials of aquaphotomics and its chemometrics approaches. *Front. Chem.* **2018**, *6*, No. 363.

(66) Han, L.; Sun, Y.; Wang, S.; Su, T.; Cai, W.; Shao, X. Understanding the water structures by near-infrared and Raman spectroscopy. *J. Raman Spectrosc.* **2022**, *53* (10), 1686−1693.

(67) Chatani, E.; Tsuchisaka, Y.; Masuda, Y.; Tsenkova, R. Water Molecular System Dynamics Associated with Amyloidogenic Nucleation as Revealed by Real Time Near Infrared Spectroscopy and Aquaphotomics. *PLoS One* **2014**, *9* (7), No. e101997, DOI: 10.1371/journal.pone.0101997.

(68) Tsenkova, R. N.; Iordanova, I. K.; Toyoda, K.; Brown, D. R. Prion protein fate governed by metal binding. *Biochem. Biophys. Res. Commun.* **2004**, *325* (3), 1005−1012.

(69) Maeda, H.; Ozaki, Y.; Tanaka, M.; Hayashi, N.; Kojima, T. Near Infrared Spectroscopy and Chemometrics Studies of Temper-ature-Dependent Spectral Variations of Water: Relationship between Spectral Changes and Hydrogen Bonds. *J. Near Infrared Spectrosc.* **1995**, *3* (4), 191−201.

(70) Hu, X.; Li, F.; Xia, F.; Guo, X.; Wang, N.; Liang, L.; et al. Biodegradation-Mediated Enzymatic Activity-Tunable Molybdenum Oxide Nanourchins for Tumor-Specific Cascade Catalytic Therapy. *J. Am. Chem. Soc.* **2020**, *142* (3), 1636−1644.

(71) Li, D.; Ha, E.; Zhang, J.; Wang, L.; Hu, J. A synergistic chemodynamic−photodynamic-photothermal therapy platform based on biodegradable Ce-doped MoOx nanoparticles. *Nanoscale* **2022**, *14* (39), 14471−14481.

(72) Ni, D.; Jiang, D.; Kutyreff, C. J.; Lai, J.; Yan, Y.; Barnhart, T. E.; et al. Molybdenum-based nanoclusters act as antioxidants and ameliorate acute kidney injury in mice. *Nat. Commun.* **2018**, *9* (1), No. 5421.

(73) Eliášová Sohová, M.; Bodík, M.; Siffalovic, P.; Bugárová, N.; Labudová, M.; Zat'ovičová, M.; et al. Label-free tracking of nanosized graphene oxide cellular uptake by confocal Raman microscopy. *Analyst* **2018**, *143* (15), 3686−3692.

(74) Ditte, P.; Dequiedt, F.; Svastova, E.; Hulikova, A.; Ohradanova-Repic, A.; Zatovicova, M.; et al. Molecular and Cellular Pathobiology Phosphorylation of Carbonic Anhydrase IX Controls Its Ability to Mediate Extracellular Acidification in Hypoxic Tumors. *Cancer Res.* **2011**, *71*, 7558−7567.

(75) Downes, A.; Elfick, A. Raman spectroscopy and related techniques in biomedicine. *Sensors* **2010**, *10* (3), 1871−1889.

(76) Wang, H.; Tsai, T. H.; Zhao, J.; Lee, A. M. D.; Ka, B.; Lo, K.; et al. Differentiation of HaCaT cell and melanocyte from their malignant counterparts using micro-Raman spectroscopy guided by confocal imaging. *Photodermatol., Photoimmunol. Photomed.* **2012**, *28*, 147−152.

(77) Stiebing, C.; Schmölz, L.; Wallert, M.; Matthäus, C.; Lorkowski, S.; Popp, J. Raman imaging of macrophages incubated with triglyceride-enriched oxLDL visualizes translocation of lipids between endocytic vesicles and lipid droplets. *J. Lipid Res.* **2017**, *58* (5), 876−883.

(78) Smith, R.; Wright, K. L.; Ashton, L. Raman spectroscopy: An evolving technique for live cell studies. *Analyst* **2016**, *141* (12), 3590−3600.

(79) Keleştemur, S.; Avci, E.; çulha, M. Raman and surface-enhanced Raman scattering for biofilm characterization. *Chemosensors* **2018**, *6*, 5.

(80) Kann, B.; Offerhaus, H. L.; Windbergs, M.; Otto, C. Raman microscopy for cellular investigations - From single cell imaging to

drug carrier uptake visualization. *Adv. Drug Delivery Rev.* **2015**, *89*, 71−90.

(81) Heraud, P.; Marzec, K. M.; Zhang, Q. H.; Yuen, W. S.; Carroll, J.; Wood, B. R. Label-free in vivo Raman microspectroscopic imaging of the macromolecular architecture of oocytes. *Sci. Rep.* **2017**, *7* (1), No. 8945, DOI: 10.1038/s41598-017-08973-0.

(82) Dorney, J.; Bonnier, F.; Garcia, A.; Casey, A.; Chambers, G.; Byrne, H. J. Identifying and localizing intracellular nanoparticles using Raman spectroscopy. *Analyst* **2012**, *137* (5), 1111−1119.

(83) Byrne, H. J.; Bonnier, F.; Efeoglu, E.; Moore, C.; McIntyre, J. In vitro Label Free Raman Microspectroscopic Analysis to Monitor the Uptake, Fate and Impacts of Nanoparticle Based Materials. *Front. Bioeng. Biotechnol.* **2020**, *8*, No. 1277.

(84) Ettinger, A.; Wittmann, T. Fluorescence live cell imaging. *Methods Cell Biol.* **2014**, *123*, 77−94.

(85) Štefík, P.; Annušová, A.; Lakatoš, B.; Elefantová, K.; Čepcová, L.; Hofbauerová, M.; et al. Targeting acute myeloid leukemia cells by CD33-receptor specific MoS_2-based nanoconjugates. *Biomed. Mater.* **2021**, *16* (5), No. 055009.

(86) Kapustová, M.; Puškárová, A.; Bučková, M.; Granata, G.; Napoli, E.; Annušová, A.; et al. Biofilm inhibition by biocompatible poly(ε-caprolactone) nanocapsules loaded with essential oils and their cyto/genotoxicity to human keratinocyte cell line. *Int. J. Pharm.* **2021**, *606*, No. 120846.

(87) Garimella, S. V.; Drozd, V.; Durygin, A. High-pressure Raman study on the decomposition of polycrystalline molybdenum hexacarbonyl. *J. Inorg. Organomet. Polym. Mater.* **2009**, *19* (3), 415−421.

(88) Seguin, L.; Figlarz, M.; Cavagnat, R.; Lasskgues, J. C. Infrared and Raman spectra of MoO3 molybdenum trioxides and MoO3 · xH2O molybdenum trioxide hydrates. *Spectrochim. Acta, Part A* **1995**, *51* (8), 1323−1344.

(89) Ou, J. Z.; Campbell, J. L.; Yao, D.; Wlodarski, W.; Kalantar-Zadeh, K. In situ Raman spectroscopy of H2 gas interaction with layered MoO3. *J. Phys. Chem. C* **2011**, *115* (21), 10757−10763.

(90) Shipp, D. W.; Sinjab, F.; Notingher, I. Raman spectroscopy: techniques and applications in the life sciences. *Adv. Opt Photonics* **2017**, *9* (2), 315.

(91) Pastorek, J.; Pastorekova, S.; Callebaut, I.; Mornon, J. P.; Zelnik, V.; Opavsky, R.; et al. Cloning and characterization of MN, a human tumor-associated protein with a domain homologous to carbonic anhydrase and a putative helix-loop-helix DNA binding segment. *Oncogene* **1994**, *9* (10), 2877−2888.